PLANNING NEEDLE PLACEMENT IN IMAGE-GUIDED RADIOFREQUENCY ABLATION OF HEPATIC TUMORS

By

Chun-Cheng Richard Chen

Dissertation
Submitted to the Faculty of the
Graduate School of Vanderbilt University
in partial fulfillment of the requirements
for the degree of

DOCTOR OF PHILOSOPHY

in

Biomedical Engineering

December, 2006

Nashville, Tennessee

Approved:

Robert Galloway, PhD

Michael I. Miga, PhD

Robert J. Roselli, PhD

Richard Shiavi, PhD

To my mother and father, who instilled in me a love of learning,

and

To my grandfather, whose ingenuity continues to be inspirational

ACKNOWLEDGEMENTS

When this research project was first presented to me by Dr. Bob, I admit failing to appreciate the complexity and richness of the topic. Only after tackling the questions posed to me did I begin to see the many avenues of inquiry that they opened. Dr. Bob had graciously and patiently allowed me to explore many of these problems at my own pace as I continually reformulated the initial project for myself. His guidance as mentor was most valuable when the progress of the research seemed slowest, always reassuring and reinforcing with wisdom. While Dr. Bob kept me focused on the big picture of the research, Dr. Miga gave me valuable advice on its theoretical aspects. I have shamelessly abused his open door policy whether to discuss a paper on the latest computational modeling techniques or to debate the interpretation of experiment results in various theoretical contexts. Many a time, I have found myself rediscovering an approach that Dr. Miga had proposed to me earlier, at a time when I could not begin to appreciate its subtlety and simplicity. I cannot credit Dr. Bob and Dr. Miga enough for overseeing the scientific rigor of this research and in training me.

The Galloway and Miga labs have been and continue to be fertile ground for emerging ideas to difficult problems. The members of the labs nurtured my academic interests both by allowing me to participate in their various projects and helping me generously with my own. They also provided me with the essential, intellectually fulfilling diversions to keep me sane through my studies.

I appreciate the advice of the other faculty of the Biomedical Engineering Department, including Bob Roselli, Duco Jansen and Rich Shiavi. The first two were instrumental in shaping my research proposal and providing constructive criticism. I am also thankful for the aid of Profs. Roselli and Shiavi in helping me set a timely defense date so that I could continue my medical education.

Julie Poulsen, RN, was a major benefactor to this research, loaning the Surgery Department's once sole radiofrequency generator to me and donating several unused ablation probes so that I could conduct my experiments. Other people in the Surgery Department, including Dr. Wright Pinson, Dr. Ravi Chari, Dr. Philip Bao, and Dr. William Chapman have been supportive of my endeavor especially in motivating my research topic and giving me much appreciated exposure to the surgical room.

I would have been lost in the frustrations of graduate research were it not for the love and support of my parents, who continued to provide me the necessary sustenance and shelter during my studies. Their reminder that this milestone would be only one of many in my life helped to keep me grounded. It also did not hurt to hear from them how much money I was not making by staying in graduate school.

Finally, this work could not be possible without the generous financial support of the NIH, in the form the of Medical Scientist Training Program grant, and from Creare Inc. Eric Friets and David Kynor from Creare have also allowed me to participate extramurally in their research project involving abdominal laser range scanning, for which I am grateful.

TABLE OF CONTENTS

LIST OF FIGURES

LIST OF TABLES

CHAPTER I

INTRODUCTION

Overview

Radiofrequency ablation (RFA) has gained widespread acceptance in the treatment of liver tumors, particularly those tumors that are unresectable. Despite the increasing clinical usage of RFA, technical challenges remain in achieving complete ablation of tumors. In hepatic applications, RFA produces ablation zones that are limited in size both as a result of tissue properties as well as constraints in ablation device design and physics. Because RFA is a focal therapeutic modality, proper placement of the RF device is an important goal in producing successful treatment in which the resulting ablation extents overlap the detectable tumor as well as a suitably defined margin which might contain undetected disease. Achieving this goal requires planning in a manner that takes into account the known physical processes which govern RF ablations. It also depends on the ability to target the device accurately to a desired location. Both of these objectives are linked, however. Indeed, accurate placement depends on having a predefined plan. In turn, a robust plan must account for the limitations in targeting accuracy. Although, these objectives have been explored in the literature as separate problems, little has been done to create a treatment planning framework which accounts for both the physics of ablation as well as the targeting constraints in device placement. This dissertation research studied this problem by applying computational modeling and image-guided techniques to RFA. In Chapter II, a method will be presented to search for needle placement that best satisfies a therapeutic goal given outcomes predicted by finite element models of ablations. The technique will be applied to simulated scenarios involving single as well as multiple ablations. In Chapter III, a phantom system will be developed to test ablation experiments using a tracked RFA. A design for the tracked device as well as a means of calibrating the tracked device will be described. The positional information from the tracked device will be fed into the model produced in Chapter II to quantify the model accuracy in predicting the spatial extents of the ablations within the phantom. Metrics to quantify the model accuracy will be introduced, and the effects of potential tracking inaccuracies will be analyzed. Finally, in Chapter IV, the sensitivity of predicted ablations to needle placement inaccuracies will be studied theoretically. A novel technique will be introduced that couples boundary element and finite element methods to obtain multiple simulations efficiently for different needle placements over a static mesh. The technique will be coupled to Monte Carlo simulations to generate a spatial map of the likelihood of ablation success. The numerical method will then be used to study sensitivity of ablation outcomes near vessels to misplacement of the RFA device.

Background and Significance

Clinical relevance

In 2002 the World Health Organization estimated 628,000 new primary liver tumor cases globally [1], of which hepatocellular carcinoma (HCC) is the most common type. Worldwide, HCCs rank as the fifth most frequent solid tumor and the fourth most common cause of cancer related mortality annually [2], with predominance especially in Asian and African nations [3]. Patients with HCCs, if left untreated, have a 5 year survival rate less than 5% [4, 5]. In the United States, HCCs are uncommon, but metastatic tumors arising from extrahepatic primary tumors are prevalent. The liver is a common site for metastatic disease from extrahepatic primary tumors, particularly from other gastrointestinal tumors, because the liver drains venous blood from all other abdominal organs [6]. A major source of these metastases comes from colorectal tumors, the second most common tumor type in the US with an estimated 146,000 new cases in 2004 [7]. An estimated 50% of these patients will develop metastases in the liver, and if left untreated, have average survival rates of 6 to 12 months [8].

In both HCC and metastatic disease to the liver, the current conventional treatment with curative intent is surgical resection [9]. Surgery can potentially provide curative outcomes for both HCC and hepatic metastases [8, 10], with 5 year survival rates between 20-40% [4], especially if a 1 cm negative margin can be achieved [11, 12]. Nevertheless, only 10-15% of patients with metastatic disease and less than 30% of patients with HCC are eligible candidates for surgical resections. Clinical reasons for excluding patients from liver resections include inadequate functional hepatic reserves, proximity of tumors to vascular and biliary structures, multifocal lesions, as well as other underlying liver diseases [13].

RFA mechanism

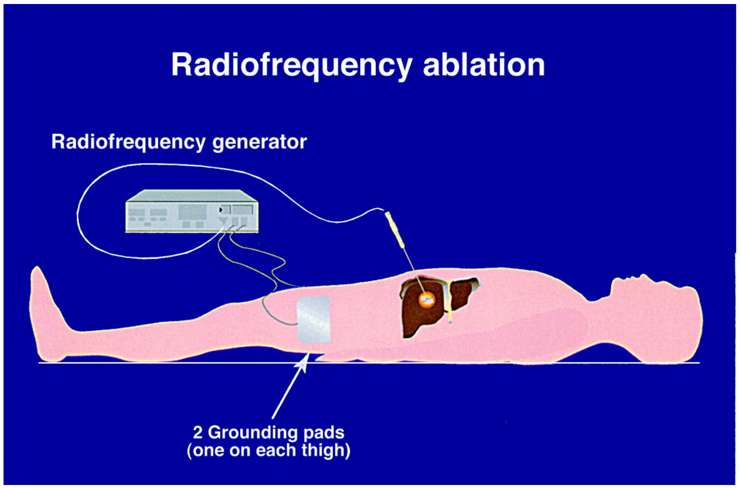

Figure I-1: Diagram depicting closed electrical circuit in RFA procedure, reproduced from [14].

Radiofrequency ablation (RFA) is currently a widely used treatment modality for unresectable hepatic tumors [15]. Among the advantages of RFA over other thermal ablative therapeutic modalities are its cost-effectiveness [16] and its low complication rates [17, 18]. 3 year survival rates have recently been reported at 50-70% for RFA treated patients [19]. As shown in Figure I-1, RFA works by inserting electrodes directly into a cancerous lesion. Typically this procedure is performed under image guidance such as ultrasound. Depending on the RFA system, additional metallic tines may then be deployed. A radiofrequency voltage source (typically, 400-500 kHz) is then applied to the electrodes relative to large dispersive grounding pads. Consequently, mobile ions in the tissue surrounding the electrodes attempt to travel in the alternating directions of the electric field. It is the movement of these ions by electrical conduction that raises the temperature of the surrounding tissue through resistive heating, which in turn causes focal thermal damage to the tissue. In a typical application of RFA, temperatures reach upwards of 100°C in the immediate areas around the active electrodes. Larger volumes of ablation around the electrodes are achieved chiefly by heat conduction from the zones surrounding the electrodes [20]. At supra-physiologic temperatures (above 45-50°C), tumors undergo coagulative necrosis, which is irreversible cellular damage caused by denatured proteins and disrupted cellular membranes. Cell death is considered instantaneous at around 60°C [4, 21-23].

RFA of large tumors

A major goal of current ablation research is in achieving larger ablations [24]. Various commercial RFA systems have been well documented for their capacity to produce spherical ablation zones of 3 cm in diameter [25]. Although the underlying therapeutic mechanisms among these systems are in principle the same, there are differences in needle design and control of power delivery. Newer electrode and RF generator designs can reportedly achieve ablation sizes as large as 5-7 cm in diameter, with each RFA procedure lasting approximately 10-15 minutes. In order to maintain sufficient power density within the target tissue, some electrodes are cooled internally and designed to infuse saline to maintain tissue conductivity [26]. More recently, methods have been explored to achieve larger ablations by simultaneously applying power to multiple RFA probes [27].

Despite these improvements in RFA system design, there have been limited successes in applying RFA towards the treatment of large tumors, typically greater than 3 cm in diameter given current RFA technology [28-30]. Attempts to treat large tumors, as reported in the literature, usually result in high local recurrence rate of the tumor. RFA achieves optimal results when treating tumors that are smaller than the maximum ablation size. Because, as is done in surgical cases, an additional treatment margin of 0.5-1.0 cm around the tumor needs to be treated in order to reduce local recurrence, tumors that are comparable in size to the ablation volume usually are not treated adequately. In a recent report in which tumors larger than 5 cm in diameter were treated with ablation zones of 3 cm in diameter, the success rate was lower than 50% [29]. The other known limitation of RFA is the failure to treat tumors that are close to thermal sinks. In particular, nearby vessels as small as 3mm in diameter can produce inadequate treatment [31-33]. This effect is described in Figure I-2.

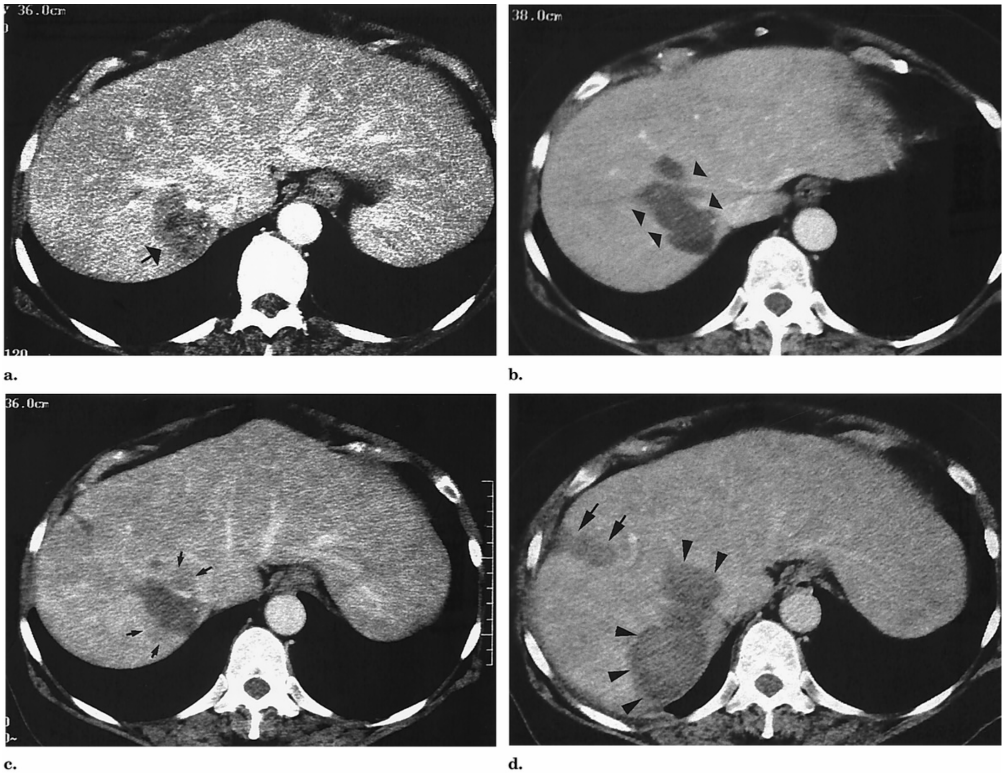

Figure I-2: Incomplete treatment of tumor surrounded by blood vessels. *a*) A preoperative CT shows the location of the tumor near large hepatic veins. *b*) Initial treatment reveals defects in the ablation zone, manifesting as irregular borders. *c*) Nine months later, a CT study reveals local recurrence as shown by arrows. *d*) Ablations were performed to treat recurring tumors. Image reproduced from [32].

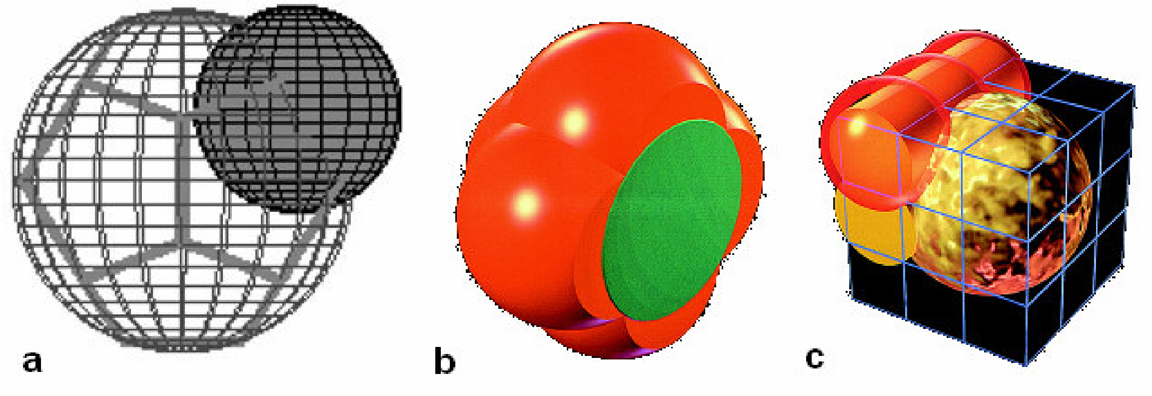

Figure I-3: ***a)*** Wireframe model of an inscribed regular dodecahedron with a sphere placed at the center of one of its faces. ***b)*** Solid model showing 6 overlapping ablation spheres arranged in a regular octahedron, with a cutaway depicting the tumor. ***c)*** A cylindrical ablation strategy in which cubes tile the treatment volume and ablation spheres are placed circumscribing each cube. Figures are reproduced from [34, 35].

Image guided techniques

One hypothesized factor contributing to the inadequate treatment of tumors is inadequate guidance and monitoring of the RFA procedure. During RFA, surgeons rely heavily on 2D intraoperative ultrasound (IOUS) for guidance and limited treatment monitoring [23]. Nevertheless, few studies have been performed to evaluate the accuracy of 2D IOUS guidance to position the RFA probe at the center of the tumor. In one study, Scott et al. reported 4.2 ± 1.4 mm and 3.5 ± 1.6 mm discrepancies between the pathologic ablation center and the center of a tumor-mimic created in porcine liver [36]. Accurate localization becomes important in particular when parts of the tumor are not visible under IOUS. Typically, an initial ablation causes gas bubble formation. The gas produces a highly echogenic effect with IOUS, which results in acoustic shadowing of all tissue deep to the ablation. If additional ablations are required, IOUS may no longer be able to detect residual tumor. Other investigators have studied ways to improve localization of the RFA probe inside the tumor. Certain methods attempt to overcome the limitations of 2D visualization inherent to IOUS by adopting 3D imaging modalities [37, 38]. Results using 3D imaging retrospectively to evaluate IOUS targeting showed that off-centered needle placement could sometimes escape detection with IOUS [39].

Other methods use preoperative images registered to the physical space of the operating field as a means of intraoperative guidance [40, 41]. This technique takes advantage of the higher resolution and contrast of MRI or CT images for accurate probe placement. By tracking the location of the RFA needle in physical space, its corresponding location in preoperative image space can be determined. The utility of this image-guided method depends, however, on achieving accurate registration of images with an organ that has few rigid anatomical landmarks, deforms nonrigidly [42] and may move substantially during the operation, whether due to breathing or due to the surgical procedure itself [43].

Planning algorithms for ablation

A few attempts have been made to devise a treatment planning system for ablation therapy. Butz *et al.* formulated a nonlinear optimization problem to select the optimal ablation zone locations [44]. Ablations zones were modeled as spheres or ellipsoids. Their method involved optimizing an objective function based on weighted sums of the ablated volume within the prescribed treatment volume and the ablated volume of healthy tissue outside of the treatment volume. The weights were selected based on the sensitivity of healthy critical structures near the tumor. Villard *et al.* similarly used ellipsoidal ablation zones to cover a given treatment volume by maximizing the number of tumor voxels covered [45]. In addition, however, the investigators allowed constraints on allowable trajectories so that the ablation probe does not place through critical structures. Another innovation was to model the heat-sink effects of liver vasculature by dynamically deforming the ellipsoidal ablation zones depending on their proximity to large vessels [46], and using the deformed shapes in optimizing placement. This deformation was achieved phenomologically, however, without relying on any specific model of the underlying physical processes.

Dodd *et al.* described a different approach using geometric analysis in order to place spherical ablation zones in such a way as to cover a spherical treatment volume completely [34]. They were able to demonstrate that spheres placed in specific patterns around the treatment volume could cover spherical treatment volumes up to 1.66 times the diameter of the ablation zone. Their results further revealed that for a 66% increase in diameter, 14 ablations would be required to be placed in precise locations, illustrating the potential logistical limitations of using overlapping spheres. Other strategies were based on using columns of ablations to achieve cylindrical ablation zones. Multiple cylindrical ablations were then used to cover the tumor. Khajanchee *et al.* also adopted a similar geometric approach using spherical ablation zones and treatment volumes [35]. Rather than attempt to cover the entire spherical treatment volume, however, this method assumed that complete ablation of the surface of the sphere would result in complete necrosis of the tumor. A polyhedron was inscribed into the treatment volume, and ablation zones were then placed at the center of each polyhedral face. Investigators were careful to note that the imprecision of current localization made use of these treatment plans risky.

A common theme in most current planning literature for RFA is the use of multiple geometric shapes to cover another simple geometric shape. Typically, these shapes are spheres or ellipsoids. However, the number of spheres required to ablate a large treatment region increases dramatically with size. This observation is corroborated by theoretical results from the discrete and computational geometry literature on packing and covering theory [47-50]. In this theoretical analysis, the primary focus is given to deriving theoretical limits to the density of coverage for a given domain and the congruent shapes used to cover it, as well as estimating the computational complexity of the problem [51]. However, the applicability of these results towards treatment planning remains unclear.

Finally, experimental validations have been conducted to fit *in vivo* ablation data to geometric models [52]. These studies employ geometric primitives (*e.g.* ellipsoids) to fit the radiological or pathological margins of the ablation. Although this study indicates that a simple shape can be used to fit ablation zones, it fails to address whether there is predictive value when applied to tumors near other local tissue heterogeneity such as blood vessels or when other needle designs are used.

Computational modeling of RFA

Despite the intuitive appeal of the geometric planning algorithms, they do not directly account for the critical physical processes known to affect ablation shapes, such as power delivery, thermal diffusion, or the heat sink effects of blood perfusion, especially in the presence of nearby vessels greater than 3 mm. In order to address these shortcomings, computational models of the physical processes in ablation are required.

Computational models have played an integral part in understanding the limitations of RFA treatment in large tumors, especially the roles that electrical and thermal properties of the liver have in affecting ablation size [53]. Models of thermal ablation typically solve Pennes bioheat equation [54] to obtain the temperature field within a region of interest resulting from a local heat source:

$$\rho c \frac{\partial T}{\partial t} = \nabla \cdot k \nabla T - h_b \left(T - T_a \right) + Q_{RF}, \tag{1.1}$$

where Q_{RF} (W/cm^2) is the heat source; T (°C) is the temperature; k (W/cm K) is thermal conductivity; ρ (g/cm^3) is the tissue density; and c (J/g K), is the heat capacity. The convective heat transfer coefficient, h_b (W/cm^3/K) models the rate of perfusion in the tissue, as arterial blood enters the tissue at a given temperature, T_a (°C), and is assumed to equilibrate immediately with the surrounding tissue. In RFA, the heat source Q_{RF} can be computed in two steps. First the electrostatic potential Φ is obtained by solving Laplace's equation with appropriate boundary conditions:

$$-\nabla \cdot \sigma \nabla \Phi = 0 \tag{1.2}$$

where σ is the conductivity of the medium. From a solution of the potential, the heat source resulting from ohmic heating can then be estimated as the time-averaged power density generated by the resulting current: $Q_{RF} = \tfrac{1}{2} \sigma \left| \nabla \Phi \right|^2$. [55]

Published numerical models of RFA vary in complexity. In a linear model, the distribution of electrical RF energy being deposited in a region is independent of the temperature distribution [56]. Nonlinear models have been developed, however, that take into account observed temperature-dependent effects on both thermal and dielectric properties [57-60]. Although not reported specifically for RFA, thermal ablative models may also incorporate changes in blood perfusion rate [61]. One common strategy to updating temperature-dependent material properties is to employ an Arrhenius model to estimate the amount of thermal damage [57], and to update the properties as a function of damage over time.

Even though sophisticated finite element models of RFA have been described, little attention has been paid to date towards experimental validation of the models specifically for RF energy sources. Nor has much work been done towards applying the models for planning needle placement. These problems have been explored for other thermal ablative modalities, however. In particular, planning based on finite element models have been described for cryosurgical applications [62-64]. Of interest are the shared features between cryosurgical planning and RFA planning, notably the need to place multiple ablation devices such that an objective function, based on the predicted temperature, is maximized within a region of interest. These investigators studied a number of technical issues regarding coupling finite models of ablation with numerical optimization methods. Of interest are their emphases on objective function design and development of strategies to reduce the computational burden, often employing phenomological methods to fit temperature distributions, and search heuristics to arrange and evaluate the device placements.

CHAPTER II

OPTIMIZING NEEDLE PLACEMENT USING FINITE ELEMENT MODELS IN RADIOFREQUENCY ABLATION PLANNING

Abstract

Conventional radiofrequency ablation (RFA) planning methods for identifying suitable needle placements typically use geometric shapes to model ablation outcomes. A method is presented for searching needle placements that couples finite element models of radiofrequency ablation together with a novel optimization strategy. The method was designed to reduce the need for model solutions per local search step. The optimization strategy was tested against scenarios requiring single and multiple ablations. In particular, for a scenario requiring multiple ablations, a domain decomposition strategy was described to minimize the complexity of simultaneously searching multiple needle placements. The effects of nearby vasculature on optimal needle placement were also studied. Compared with geometric planning approaches, finite element models could potentially deliver needle placement plans that provide more physically meaningful predictions of therapeutic outcomes.

Introduction

Focal thermal ablative techniques have become widely adopted for the treatment of solid tumors. Examples include laser ablation [65], cryoablation [66], high intensity ultrasound [67], and radiofrequency ablation [15]. For ablation treatments to be successful, the extent of the ablated volume must overlap entirely the detectable tumor volume as well as a suitable margin that contains possible occult disease. Although the physical mechanism of heat generation differs with each modality, the extent of the resulting ablation depends for all cases on the placement of the ablation device with respect to the targeted treatment volume. Consequently, controlling the placement of the device is a factor in producing successful ablative therapy.

The focus of this study is on the application of radiofrequency ablation (RFA) in treating unresectable tumors of the liver. RFA works by inserting electrodes directly into a cancerous lesion. Radiofrequency currents (typically, 400-500 kHz) delivered through these electrodes produce resistive heating, and the resulting temperature increase causes focal thermal damage to the tissue. In a typical application of RFA, temperatures reach upwards of 100°C in the immediate areas around the active electrodes. Above a critical temperature (typically above 50°C), tumors undergo coagulation necrosis, caused by irreversible cellular damage in the form of protein denaturation and disruption of cellular membranes. Cell death is considered instantaneous at around 60°C [21]. In the course of an RFA treatment, the volume of ablated tissue increases as heat conduction distributes higher temperatures further into the tissue. In typical commercial RFA systems, a 3-5 cm spherical ablation zone is expected. Nevertheless, ablation of large tumors has proven to be unreliable [28, 68] with high local recurrence rates. Although multiple ablation strategies to create larger ablations have been employed clinically [69], the investigators cited a need for better intraoperative guidance, as well as an appreciation of local physiological factors that affect ablation outcome

Treatment planning of RFA device placement attempts to determine the position and orientation of the device relative to the targeted tissue that would maximize the therapeutic outcome as predicted by a model of radiofrequency ablation. At present, models of radiofrequency ablation used in treatment planning have largely relied upon geometric assumptions of the final ablation extents, typically spheres or ellipsoids [34, 44, 69, 70]. The observed size and shape of RF ablations in clinical data show, however, significant variability in size and geometry [71], and simulation studies using computational models of RFA have demonstrated dependence of ablation extents on a number of physical parameters [27, 58]. These variations in ablation extents represent phenomena not readily predicted by geometric shapes. Further compounding this problem is the irregular distribution of thermal sinks in the liver, particularly vessels that are larger than 3 mm in diameter [32]. These vessels have been shown to remain patent during treatment, and their proximity to a treatment region reduces the local ablation extents. Consequently, variability in ablation volume and spatial extent is expected even within a single patient as the device is placed in different locations within the target organ. More recently, investigators have attempted to incorporate patient-specific anatomical information into planning, as well as propose methods for modifying the assumed ablation geometries in the presence of nearby vessels [70]. However, these methods are based on phenomenological approximations of the underlying physical processes, and thus make use of parameters that are not necessarily physically meaningful.

In this paper, a method is presented which uses finite element models (FEMs) of radiofrequency ablation to predict ablation outcomes for the purpose of planning needle placement. Currently existing computational models of RFA are used to evaluate static geometries. The models will be extended to allow evaluations of multiple needle placements via dynamic remeshing. Then, a strategy will be described to optimize the FEM predicted ablation result over the space of allowable needle placements in a manner that minimizes the number of FEM evaluations.

Methods

Finite element model

Model geometries

The treatment domain and needle geometries used in all simulation experiments are shown in Figure II-1. The needle is modeled after the RITA Starburst XL RFA device (Rita Medical Systems, CA) in which the expandable needles have been deployed to the manufacturer's "2 cm" setting. The positions of the tips of the nine tines were measured relative to the tip of the trocar housing the electrodes. Then, circular arcs are used as skeletons to connect the tine tips to the trocar tip. A circle 0.42 mm in diameter is extruded along the skeleton to generate the three dimensional tines.

The geometries each have a local coordinate system. For the needle, the origin is located 1.5 cm proximally from the tip of the center tine. The *z*-axis is defined to be parallel to the shaft of the needle, and the *y*-*z* plane was arbitrarily chosen to contain one of the nine

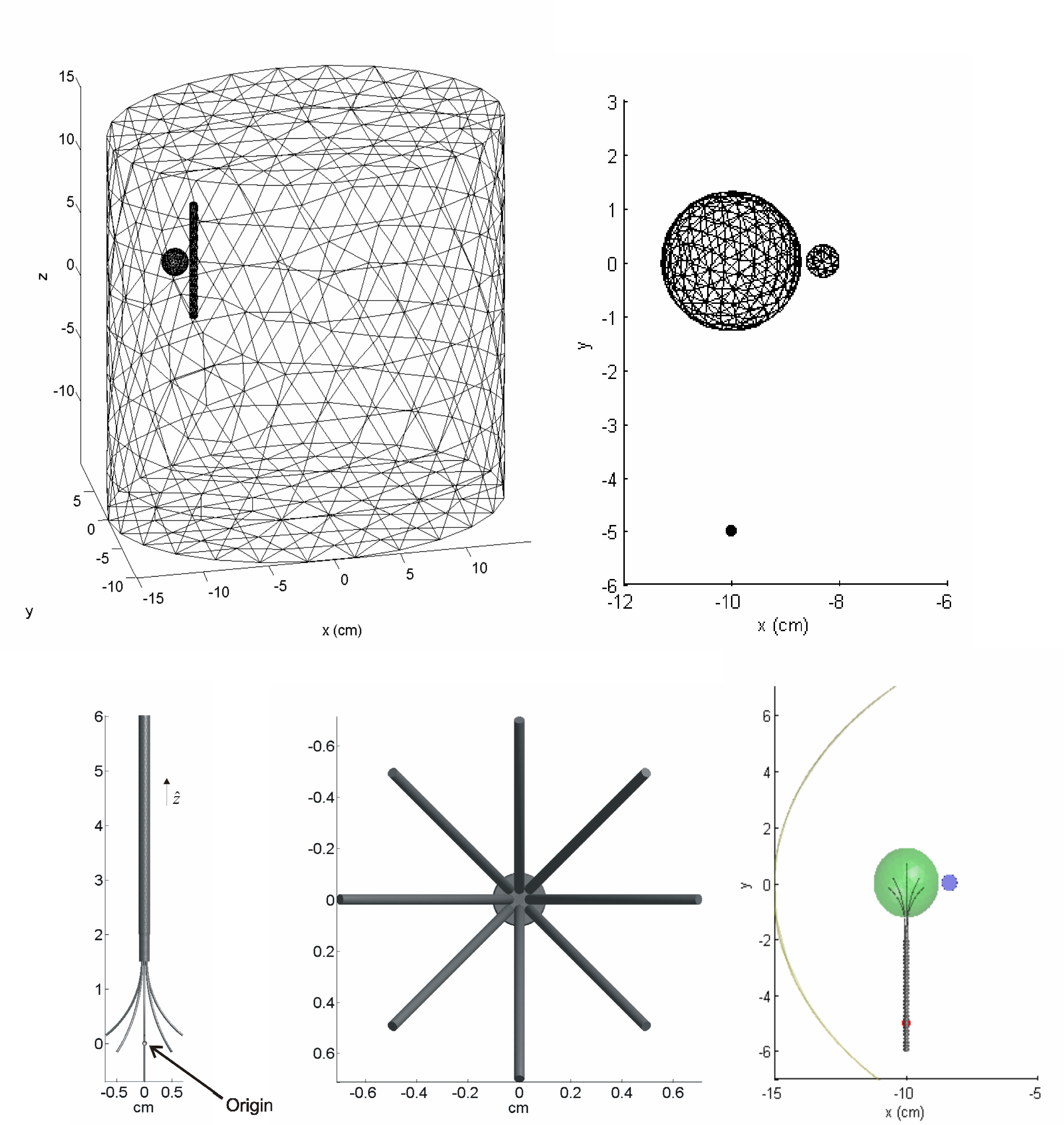

Figure II-1: (*left*) Wireframe model of the domain geometry in the global coordinate system. (*right*) Close up of the model to show, starting from top left and going clockwise: a 2.5 cm tumor, a 0.6 cm vessel, and the designated entry point for all needle placements,. The centroids of each of the three objects are placed on the *z* = 5 cm plane. (*bottom*) The surface model of a commercially used ablation device, along with its local coordinate system. The right most plot shows the placement relative to other geometries, used in all simulation epxeriments tines. In the treatment domain, the origin is located at the centroid of the outer cylinder representing the human torso. In simulation experiments, the tumor centroid is placed at coordinates (-10 cm, 0 cm, 5 cm). If a tumor is modeled, it is has a 2.5 cm diameter. In simulations involving vessels, a 6 mm cylinder running parallel to the global *z*-axis is placed such that its centroid is at coordinates (-8.6 cm, 0 cm, 5 cm) if no tumor is present, or (-8.35 cm, 0 cm, 5 cm) if a 2.5 cm tumor is present.

The allowable needle placements were constrained to simulate current RFA needle placement techniques. The needle is inserted through a prescribed entry point $\mathbf{t}_e$ (illustrated in Figure II-1), with the goal of reaching a destination point after determining the correct trajectory. In all simulations, $\mathbf{t}_e$ is given the coordinates (-10 cm, -5 cm, 5 cm). The depth of insertion and the orientation of the needle relative to the entry point are then allowed to vary freely, giving only 4 degrees of freedom as all transformations applied to the needle are assumed to be rigid about the origin of the needle. Thus, for any point $\mathbf{x}$ given in the local coordinates of the needle, the transformation, $\mathcal{T}$, to the global coordinates of the domain is defined by:

$$\mathbf{y} = T(\mathbf{x}) = R(\mathbf{x} - d\,\hat{\mathbf{z}}) + \mathbf{t}_e, \tag{2.1}$$

where *d* is the depth of insertion, $\hat{\mathbf{z}}$ corresponds to the axis of the needle, and $\mathbf{R}$ is a rotation matrix parameterized by sequential rotations about the *x*, *y*, and *z*-axes of the domain (*i.e.* $\mathbf{R} = \mathbf{R}_x(\phi_x)\mathbf{R}_y(\phi_y)\mathbf{R}_z(\phi_z)$). To simplify future discussion, a parameter vector $\boldsymbol{\theta}$ is defined, whose elements are *d* and the three Eulerian angles:

$$\boldsymbol{\theta} = \left[d, \phi_x, \phi_y, \phi_z\right]. \tag{2.2}$$

In all simulation experiments, $\boldsymbol{\theta}$ = [5.0 cm, 90°, 0°, 0°], resulting in a configuration shown in Figure II-1.

For every new needle position in which the FEM model needs to be evaluated, the entire domain is remeshed. A noncommercial meshing software package, Tetgen [72], was incorporated in order to generate volumetric meshes from an input surface mesh using constrained Delaunay tetrahedralization. This software was further modified to include routines for repairing intersecting surface meshes that may result, for instance, from the needle penetrating other structures such as the outer boundaries of the domain or the internal spherical surface representing the treatment region. Typically, 200 to 250 thousand tetrahedral elements are generated in discretizing the domain, and 40 to 50 thousand nodes are required.

Constitutive equations

Computational models of thermal ablation usually solve Pennes bioheat equation to obtain the transient temperature fields as a result of a local heat source:

$$\rho c \frac{\partial T}{\partial t} = \nabla \cdot k \nabla T + h_b \left(T - T_a \right) + Q_{RF}, \tag{2.3}$$

Q_{RF} (W/cm^2) is the heat source; T (°C) is the temperature; k (W/cm K) is thermal conductivity; ρ (g/cm^3) is the tissue density; and c (J/g K), is the heat capacity. The convective heat transfer coefficient, h_b (W/cm^3/K) models the rate of perfusion in the tissue, as arterial blood enters the tissue at a given temperature, T_a (°C), and is assumed to equilibrate immediately with the surrounding tissue. The convective coefficient, h_b, is defined to be $h_b = \rho_b c_b w_b$, where the subscript b indicates properties specific to blood, and w_b is the perfusion rate (mL/mL/s). All material coefficients are defined in Table II-1. The heat source, Q_{RF} can be approximated by first solving the electrostatic problem with appropriate boundary conditions:

$$-\nabla \cdot \sigma \nabla \Phi = 0, \tag{2.4}$$

where σ(S/cm) is the conductivity of the medium, and Φ(V) is the electrostatic potential. Given Φ, the heat source is then estimated as the time-averaged power density generated by the resulting current: $Q_{RF} = \left({P_{set}}/{P_0} \right) \frac{1}{2} \sigma \left| \nabla \Phi \right|^2$, where P_0 is the input power resulting from 1.0 V applied to the needle, and P_{set} is the desired power setting. In order to solve the coupled partial differential equations, most investigators have employed the finite element method [53, 56, 73, 74]. FEM models for radiofrequency ablation typically solve the electrostatic problem over a single meshed domain that is shared with the thermal problem. As a matter of convenience, a single mesh shared for both equations allows the estimated power deposition from the electrostatic equation to be coupled directly into the FEM formulation of the thermal problem without additional interpolation steps.

Boundary conditions are specified as follows. For the electrostatic problem, the outer surface except the bottom face is prescribed an insulative, no flux condition. A constant 1.0 V Dirichlet condition is applied on the conductive electrodes, and ground is placed on the bottom face. The total power P_{set} was set to 20 W, and the entire ablation was run for 10 minutes, after which the power was set to 0 W. For the thermal problem, the cylindrical outer surface is given an adiabatic, no flux condition, whereas the top and bottom faces are preset to 37°C. If a vessel is modeled, the vessel surface is also prescribed a constant temperature of 37°C.

Table II-1: List of material properties used in RFA simulation. Values represent the initial properties used in the simulations. As simulations proceed, the temperature-dependent properties change.

Properties	Symbol (units)	Value	Reference
Thermal conductivity (human liver)	k (W/cm·K)	5.12e-3	[73]
Density (human liver)	ρ (g/mL)	1.06	[73]
Heat capacity (human liver)	c (J/g·K)	3.6	[73]
Density (blood)	ρ_b (g/mL)	1.0e-3	[73]
Heat capacity (blood)	c_b (J/g·K)	4.18	[73]
Perfusion	w_b (mL/mL/s)	6.4e-3	[73]
Electrical conductivity (human liver)	σ (mS/cm)	3.33e-3	[73]
Activation energy	ΔE_a (J)	6.28e5	[75]
Activation factor	A (s^{-1})	3.1e98	[75]

Finally, a measure of tissue damage accumulated over the course of the ablation is computed. A suitable metric is the Arrhenius damage index, which has been previously employed by investigators [53, 75, 76] to predict the resulting thermal damage to the tissue. In this work, a related parameter to the damage index, namely the survival fraction is used. It is given by:

$$\frac{\partial \omega(\mathbf{x},t)}{\partial t} = -A\exp\left(-\frac{\Delta E_a}{RT(\mathbf{x},t)}\right)\omega(\mathbf{x},t), \tag{2.5}$$

with the initial condition that $\omega(\mathbf{x},t_0)=1$. The Arrhenius survival function, ω, can be interpreted as the ratio of viable cells to total cells inside a region of space. Thus, for $\omega = 1$, the tissue is considered viable, and when $\omega << 1$ the tissue is considered to have undergone coagulation necrosis. In this work, the threshold used to demarcate the onset of coagulation necrosis is $\omega_0 = e^{-1}$ or approximately 37%.

As suggested previously by other investigators [53, 55], this model implements temperature dependent electrical conductivity and perfusion to account for relevant property changes observed in clinical ablations. The electrical conductivity of ionic solutions increases at a rate of 2%/°C [77]. On the other hand, perfusion decreases as temperature rises because of coagulation of microvasculature. There is, however, no consensus model of how this behavior should be modeled. In this work, the perfusion is scaled linearly by the local Arrhenius survival fraction $h_b(\mathbf{x},t)=h_{b0}\omega(\mathbf{x},t)$, in a manner similar to that proposed in [75, 78]. Thus, at the start of the simulation, the convective term is given in the table above, and tends towards zero as ablation proceeds. The temperature dependence of other parameters has been neglected because their inclusion in the model would produce relatively small changes in the final temperature [79]. As the mesh is regenerated for each needle placement, routines are implemented to assign appropriate material properties to each tetrahedral element.

In order to solve the system of equations, an external iterative solver package (PETSc, [80]) was used. The transient temperature solution was obtained over 15 minutes via a fully implicit time-stepping scheme with 15 second intervals. Temperature-dependent properties were updated by using the temperature distribution from the previous iteration. A constant power setting was imposed on the electrostatic problem. At every time step, the electrostatic field was updated with the new conductivity properties. The resulting power density was then scaled so that the total power in the domain was 20.0 W. This setting was predetermined by so that the maximum temperature in the domain at the end of ablation, 10 minutes after start of the simulation, did not greatly exceed 100 °C. After 10 minutes of ablation, the applied power was set to zero.

Optimization algorithm

Objective function

In this study, the objective is to minimize the predicted Arrhenius survival fraction, ω, in a weighted sense everywhere in the region of interest (ROI), at the end of the simulation:

$$\mathscr{J} = \int_{ROI} W(\mathbf{x})\,\omega(\mathbf{x}, t_f)\,d\mathbf{x}, \tag{2.6}$$

in which the weighting term, W, is given to be,

$$W(\mathbf{x}) = \begin{cases} 1, \mathbf{x} \in \textit{tumor} \\ 0, \textit{otherwise} \end{cases}. \tag{2.7}$$

The objective function as defined above represents the residual tumor volume that is viable after ablation. Minimizing $\mathscr{J}$ is tantamount to reducing the chances that local recurrence may occur because of residual tumor cells. In the simulation experiments, the time to observe the Arrhenius was 5 minutes after power shut off, or $t_f = 15$ minutes.

Search method

In order to search for the needle position that optimizes the given objective function, the resulting ablation zone for each needle position needs to be estimated. A straightforward implementation would reevaluate the FEM model for each new needle position to recompute the objective function. Because the FEM model is a computationally expensive process, however, a method is required to minimize the number of FEM model reevaluations. In this work, the strategy is to approximate the FEM solution as a field that transforms rigidly with the needle. In this manner, the problem can be recast as an image processing problem. Computationally, the objective function (2.6) can be viewed as the correlation of two scalar volumetric images. The first "image," W, describes the relative importance of a point in the target domain in the objective. The second "image," ω, represents the likelihood of achieving complete ablation at a given position relative to the needle. Thus, the optimal localization of the needle is one that transforms the ω image to be minimally correlated with the W image, subject to constraints given in (2.1):

$$\boldsymbol{\theta}^* = \arg\min_{\boldsymbol{\theta}} \int_{ROI} W(\mathbf{x})\,\omega\left(\delta\mathcal{T}(\mathbf{x};\boldsymbol{\theta}), t_f\right) d\mathbf{x} \tag{2.8}$$

where $\delta\mathcal{T}$ is the incremental transformation from the initial transform of the needle, $\mathcal{T}(\boldsymbol{\theta}_0)$, as given by

$$\delta\mathcal{T}(\boldsymbol{\theta}) = \mathcal{T}(\boldsymbol{\theta}) \circ \mathcal{T}^{-1}(\boldsymbol{\theta}_0). \tag{2.9}$$

Implicit in the proposed strategy is the assumption that the ablation shape does not change significantly over small perturbations of its orientation and position. The justification comes from the observation that the RF power is deposited chiefly within a few millimeters [81] of the conductive electrodes, and in particular near the tips of the tines. Thus, the regions of highest power density tend to vary closely with the position and orientation of the needle. If the domain is homogeneous and the relevant boundary conditions sufficiently far away, then the resulting ablation shape would be largely invariant with respect to the needle position and orientation. Nevertheless, in clinically relevant applications such as in the liver, there is in fact local material inhomogeneity, and thermal and electrical boundary conditions may be nearby. Thus, spatial variability of the ablation with respect to the needle is expected as the needle is relocated during the search process. To correct for deviations from the assumption in the image correlation problem, the finite element model is reevaluated periodically to update the image, ω. To implement this strategy described above, the following steps are taken. At iteration, m, of the global search loop, the survival distribution, ω_m, is obtained by reevaluating the FEM problem. Then, ω_m is sampled around the present orientation and position of the needle to form a discrete image, $\boldsymbol{\omega}_{\mathrm{m}}$ The samples form a 6 cm cubic Cartesian grid of 1 mm cubic pixels, a size sufficiently large enough to capture the expected ablation extents. This "needle" grid is axis-aligned with the local reference frame of the needle and centered about the origin of the needle. Sampling of the tetrahedral mesh at these transformed grid points requires multiple point location queries, which are facilitated by construction of a search tree that sorted the tetrahedra of the meshed domain into rectangular bins.

A second set of pixels is used to sample the weighting function, *W*, defined over the region of interest to generate the discrete image $\mathbf{W}_{\mathrm{m}}$. These pixels from the "domain" grid are also sampled on a Cartesian grid of the same size as that of $\boldsymbol{\omega}_{\mathrm{m}}$, but are axis-aligned to the global coordinates, and centered on the region of interest. The algorithm then enters a local search loop, where at each iteration *n* of the loop a new set of placement parameters is determined in an attempt to minimize the discretized form of the objective function:

$$\mathcal{J}_{k,n} = \sum \mathbf{W}_k\left(\mathbf{x}\right)\boldsymbol{\omega}_k\left(\delta\mathcal{T}\left(\mathbf{x};\boldsymbol{\theta}_n\right),t_f\right). \tag{2.10}$$

When the transformed pixels of the image $\mathbf{W}_{\mathrm{m}}$ do not fall on the grid points of the transformed image $\boldsymbol{\omega}_{\mathrm{m}}$, linear interpolation of the sampled grid is used to obtain corresponding values of $\boldsymbol{\omega}_{\mathrm{m}}$.

The optimization method for the image correlation is steepest descent [82]. The gradient of the objective function, $\nabla_{\boldsymbol{\theta}}\mathcal{J}$, is readily achieved analytically from (2.10). Termination of the optimization is based on gradient magnitude and relative change in sequential values of $\mathcal{J}$. Upon termination of the image correlation, the FEM model is reevaluated at the most recent value of $\boldsymbol{\theta}$. In this manner, multiple rounds of FEM evaluation and image correlation minimization are performed until the search converges to a solution.

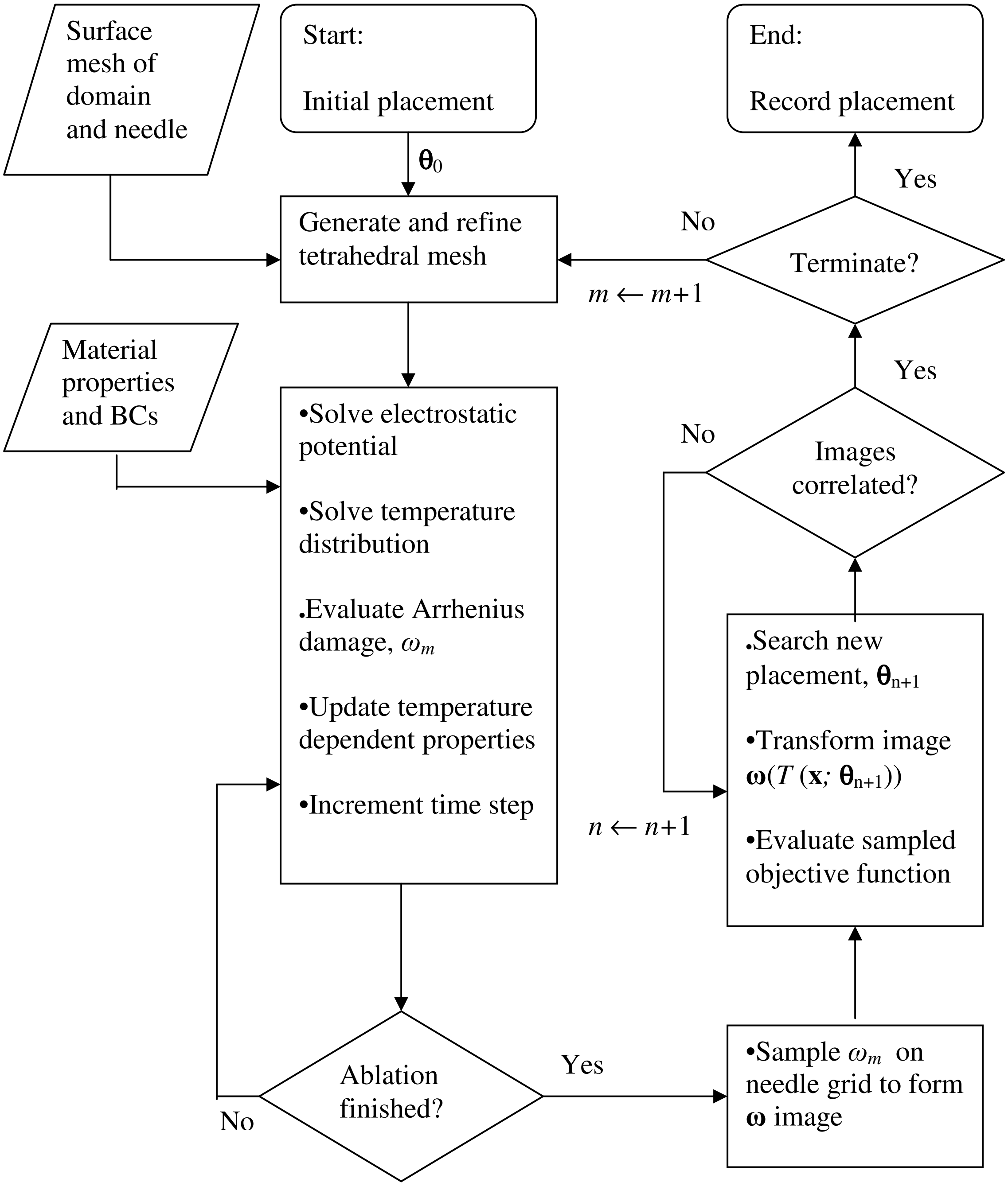

Figure II-2: Flowchart of optimization algorithm.

Termination criteria

The global search loop, which includes alternating rounds of image correlation minimization and FEM evaluation, is terminated upon reaching the maximum number of iterations prescribed. Experience with the algorithm suggests that typically no more than 10 global search steps are required. The search is also stopped if the maximum displacement of all tine tips is less than 0.01 cm between subsequent steps. Finally, in order to prevent oscillatory behavior (*i.e.* sequential steps which produce oscillatory objective function values), the search is terminated whenever the current function evaluation exceeds the previous function evaluation. This behavior occurs most often when the needle placement is already near a local optimum, at which point numerical noise (*e.g.* from FEM discretization and sampling of the solution) is the major contributor to variations in the subsequent function evaluations. The algorithm is summarized in Figure II-2. All algorithms were implemented in C++ on a Win32 platform using a 3.4 GHz Pentium 4 processor with 2 Gbytes of RAM. Runtime for a typical optimization is less than 2 hours.

Simulation experiments

Single ablations

In order to test the robustness of the optimization algorithm, the following evaluation method was devised. An ablation was simulated with an initial needle placement, and the resulting ablation zone segmented using the ω_0 threshold. All of the points in this segmented ablation were designated to be "tumor". The initial needle placement was then perturbed along each of the four degrees of freedom, as reported in

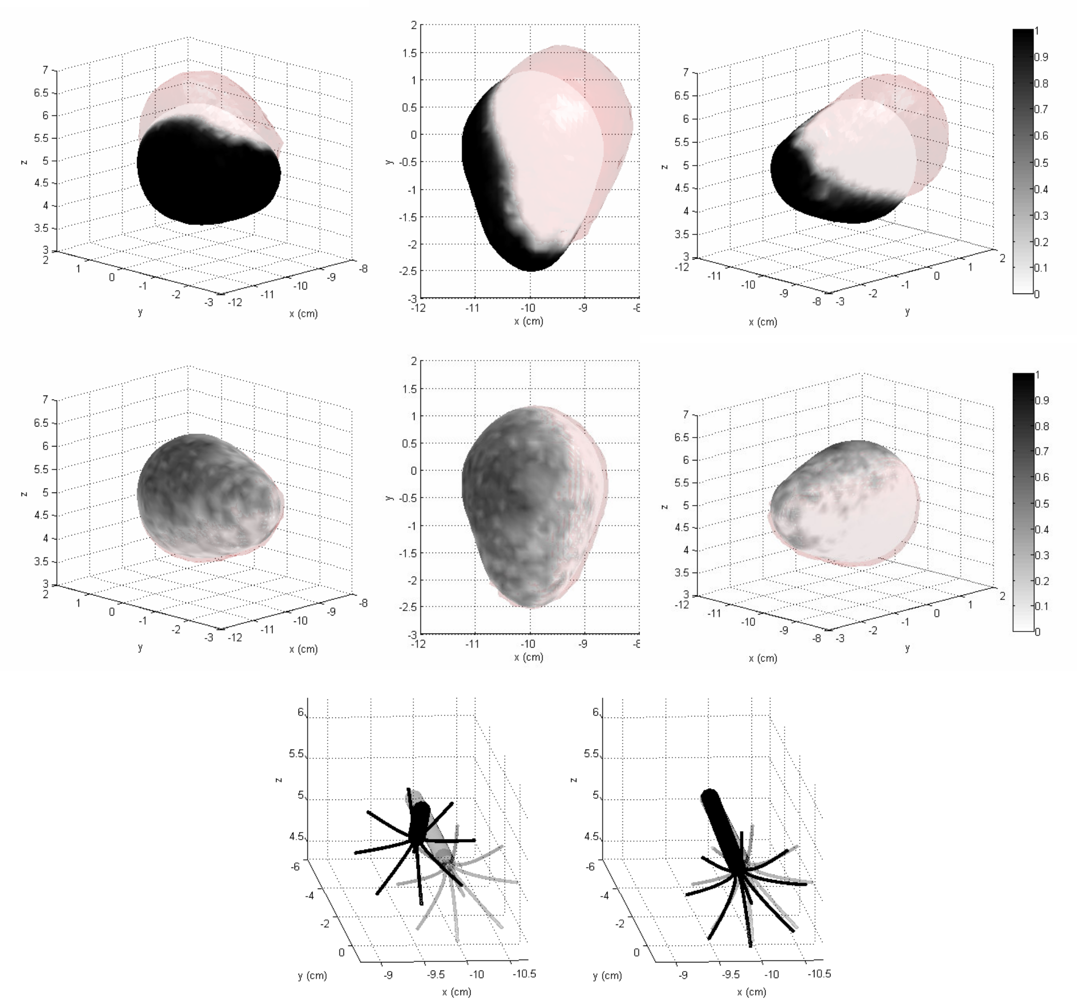

Figure II-3: (*top row*) Ablation outcomes of perturbed needle position. The solid shape is the region corresponding to an ablation from an initially placed needle, whereas the translucent shape is the current ablation from a needle perturbed from the initial placement. Shading of the ablation surface depicts unablated (black) and successfully ablated regions(white). The three figures going from left to right depict the result from lateral, superior, and medial views. (*middle row*) Recovered ablation result after optimization of needle placement. Figures correspond to same view as in top row. (*bottom row*) Comparison of perturbed needle position on the left, and recovered needle position on the right. The lightly shaded needle is the original needle placement which created the solid ablation.

Table II-2. For each perturbed needle placement, the optimization algorithm was executed to determine if the "tumor" region could be covered, and thus recovering the original needle placement. This test was performed for two geometries, designated case 1 and 2. The only difference between the cases is the presence of a 6 mm vessel in the latter.

Table II-2: Tabulated results of single ablation experiments.

	Vessel absent				**Vessel present**			
$\mathcal{J}_{init}$ (cm^3)	0.43				0.40			
$\mathcal{J}_{perturbed}$ (cm^3)	4.9				4.2			
$\mathcal{J}_{opt}$ (cm^3)	0.65				0.36			
$\Delta\left(d,\phi_x,\phi_y,\phi_z\right)$, perturbed (mm, deg)	5.0	-9.57	5.73	5.73	5.0	-9.57	-5.73	5.73
$\Delta\left(d,\phi_x,\phi_y,\phi_z\right)$, optimized (mm, deg)	-1.0e-3	0.91	0.86	4.34	3.7e-2	0.10	0.21	8.10
Mean $\left\|\Delta x\right\|_{tine}$ (mm), perturbed	9.1				9.1			
Mean $\left\|\Delta x\right\|_{tine}$ (mm), optimized	1.2				0.91			

The optimization results for both cases were able to recover the original needle position to within millimeter accuracy. The algorithm reported a lower objective function, $\mathcal{J}_{opt}$, than the perturbed function value, $\mathcal{J}_{perturbed}$, and was comparable to the unperturbed initial value, $\mathcal{J}_{init}$ (see Table II-2). The result for case 1 (without the vessel) is shown in Figure II-3, and it is evident that the optimization program was able to relocate the needle so that the optimized ablation covered the initial ablated region. Despite this improvement, however, the result showed a slight asymmetry in coverage on the region surface, where one side is ablated more completely than the other. In ablation

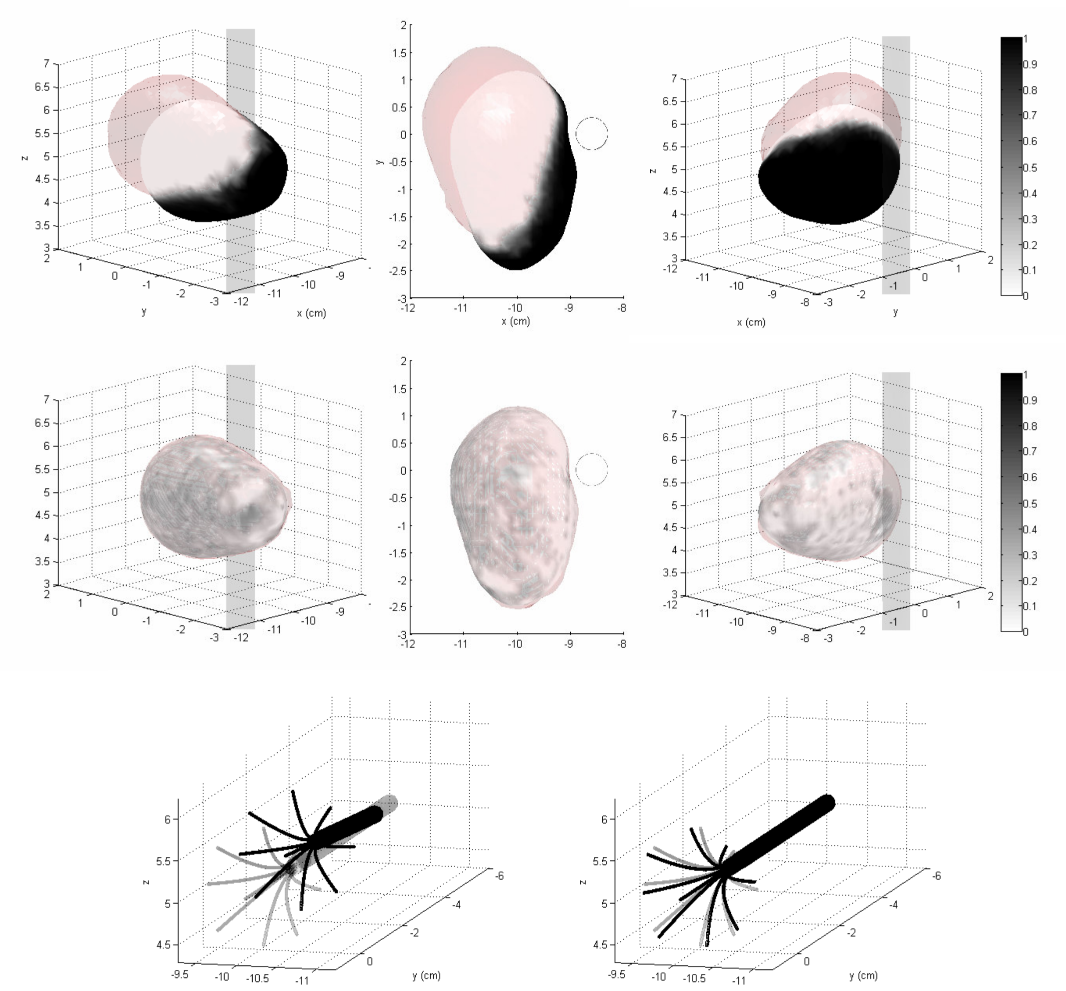

Figure II-4: Same arrangement as in Figure II-3 except for the additional presence of a 6 mm vessel.

experiments where the optimization method was executed simply on the unperturbed needle (results not shown), the optimizer also generated similar asymmetry in the final ablation, as is reported here. This result is likely due to numerical artifacts caused by sampling the FEM solution ω onto a Cartesian grid. Because the survival distribution transitions sharply between 0 and 1 in space, the sampling process could cause a misrepresentation of the local ablation at the margin. This problem may be resolved by increasing the resolution of the sampling grid, or by postprocessing the sampled image $\boldsymbol{\omega}$, such as applying smoothing filters. Nevertheless, despite this sensitivity to sampling error, the results are still reasonable considering that this experiment represents worst case scenarios in which the "tumor" is as large as the ablation. Furthermore it is not a consistent error, as comparatively speaking, the scenario for case 2 (with a vessel present), shown in Figure II-4, produced better results. The results also show that ablations are fairly insensitive to rotation about the shaft of the device (*i.e.* ϕ_z). Consequently, the optimizer is generally unable to recover the original shaft roll.

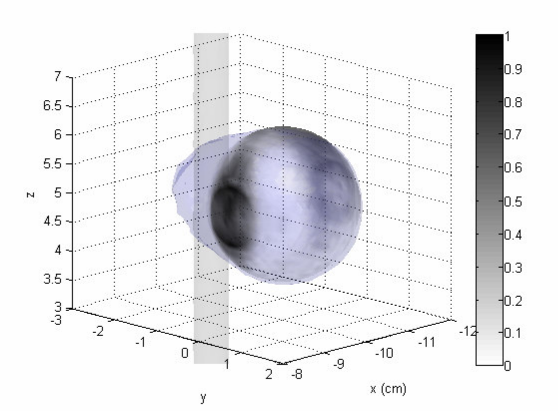

Figure II-5: Results from single ablation of 2.5 cm tumor with a nearby 6 mm vessel. The surface map shows nonablated areas (dark shade) around the periphery of the tumor, particularly near the vessel.

Multiple ablations

Table II-3: Multiple ablation results. The target volume refers to the volume of either the tumor section or the entire tumor. The last column describes the mean tine shift from the optimized single ablation placement.

	Target Volume (cm^3)	Ablation Volume (cm^3)	$\mathscr{J}_0$ (cm^3)	$\mathscr{J}_{opt}$ (cm^3)	mean $\left\|\Delta x\right\|_{tine}$ (mm)
Ablation 1	3.1	10.5	.27	6.4e-6	5.9
Ablation 2	3.1	12.1	.30	8.4e-4	3.8
Ablation 3	3.1	11.8	.40	1.8e-4	4.2
Combined	9.2	18.6	.97	2.5e-4	--
Single	9.2	11.9	.97	2.3e-1	--

While using the same external geometry as in the single ablation experiments above, a 2.5 cm spherical treatment instead was placed 1 mm away from a 6 mm vessel. Optimal planning using a single ablation resulted in ablated regions on the periphery of the spherical tumor, as shown in Figure II-5. In order to plan multiple ablations, the treatment region was first decomposed into three equal sections as depicted in Figure II-6. Needle placement was optimized independently for each section, and the resulting ablations were combined by multiplying the individual survival distributions (or equivalently, adding the logarithm of the survival distributions). Compared to the original single ablation, the results are markedly improved in which the predicted residual tumor volume is orders of magnitude smaller than for the single ablation case. As listed in Table II-3, the combined ablations create an ablation that is nearly twice that of the tumor volume, and a 56% increase over the volume of the single ablation.

It should be noted that only three ablations were required to generate a larger ablation zone. In planning with geometric spheres, investigators have noted that theoretically at least four ablation spheres are necessary to achieve an ablation of a spherical tumor that is larger than each ablation sphere [35]. The present result is possible because the predicted ablation geometry is shaped like a teardrop. Compared with a sphere, the teardrop shape is elongated along the axis of the RFA device and thus

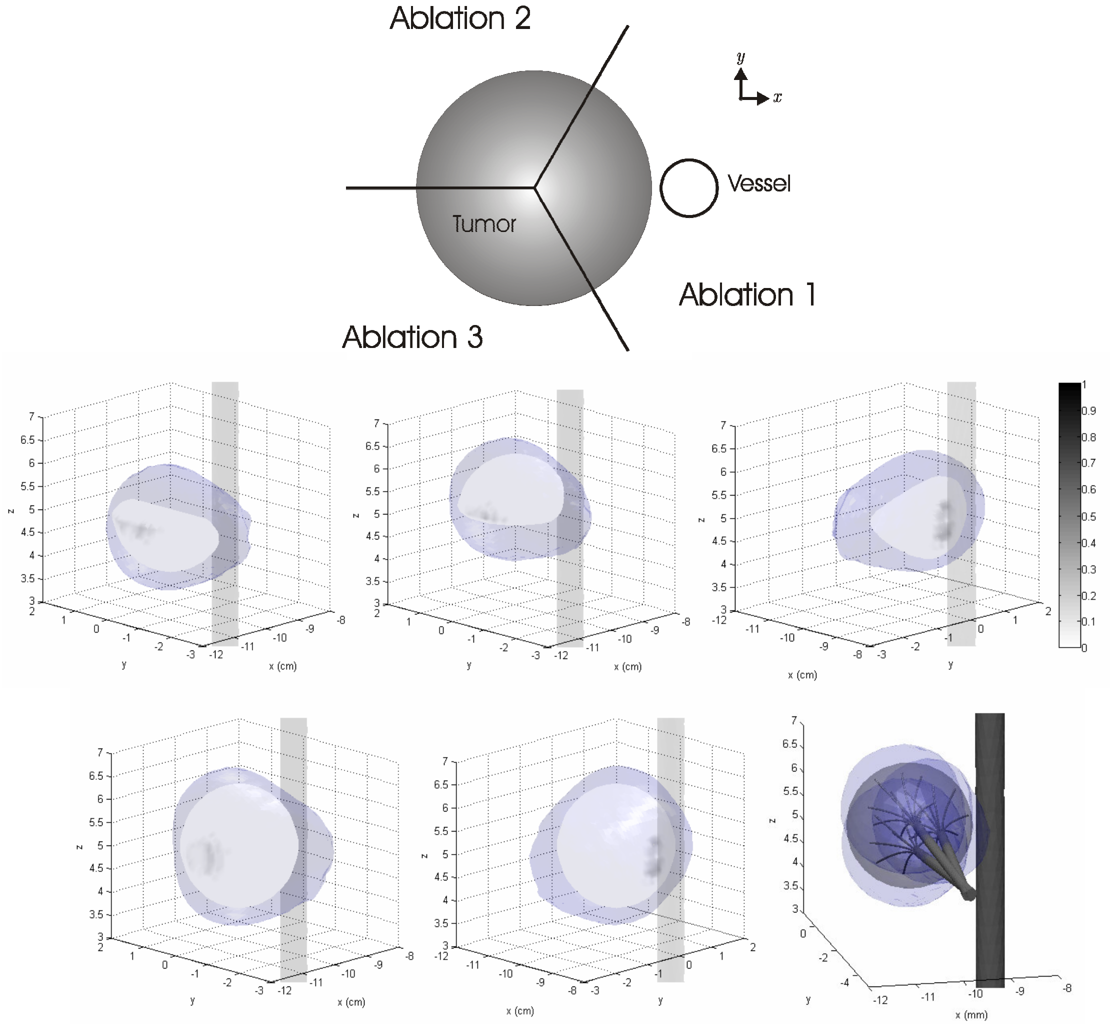

Figure II-6: (*top row*) Schematic of decomposed tumor domains in order to facilitate multiple ablation. Ablation of each wedge is planned independently of the other. (*middle row*) Results of ablation planning for wedges that correspond, going from right to left, to Ablations 1 to 3, as labeled above. (*bottom row*) Combined ablations shown in lateral and medial views. The right most figure shows the optimized needle placements.

is capable of covering wedge-shaped sections as used in this experiment. Another interesting observation is the net change in needle placement to achieve the simulated outcome. In geometric planning that uses spheres as ablation models, the plan would expect to place the probes symmetrically within a spherical tumor. In the results described above, however, the arrangement of probes is asymmetric, with the probe ablating the section closest to the vessel being displaced furthest from the optimized single ablation placement. The increase in displacement is needed to ablate the tumor margin closest to the 6 mm vessel, so that more power can be deposited near the vessel wall.

Discussion

In this paper, a method has been described to automate searches of optimal needle placement for radiofrequency ablation. This technique potentially enhances the ability of clinicians to design patient-specific plans by using not only patient anatomy but also relevant parameters that are physically meaningful and predictive. The method builds off of the theoretical observation that over small perturbations to needle parameters, the ablation shape varies slowly. Thus, an efficient search method can be developed by assuming that the ablation shape transforms rigidly with the RFA device. To account for real world scenarios in which thermal and electrical boundary conditions affect ablation shape locally, the search routine is updated periodically by reevaluating the RFA model to obtain a more accurate representation of the ablation shape. In this manner, the RFA model continues to inform the search process, but the number of model evaluations is minimized. The results presented suggest that the method is capable of optimizing needle placement.

A feature of the proposed optimization method is that it is independent of the specific FEM model used to predict the ablation outcome. Indeed, improvements can be made to the model to include, for instance, a more detailed analysis of local blood flow [83] to account for the heat sink effect of vasculature. Other commercial RFA probes may also be incorporated into the proposed search framework, along with the specific power control methods used in the design, since the method does not presume any *a priori* shape to the ablation. This search strategy could itself be integrated into larger search problems that include additional surgically relevant problems. For instance, in the method described, the entry point was fixed in the optimization scheme. Nevertheless, the entry point may also be incorporated into the planning problem, in order to identify, for instance, the best trajectory to avoid critical organs or intervening vasculature. In particular, this work could potentially enhance the planning framework previously presented by these investigators [70]. Another manner of incorporating this work into existing literature is in the use of multiple ablation planning strategies [34, 35]. Planned placements using, for instance, geometric shapes may be further refined using this framework by decomposing the tumor domain in a manner proposed in this work. Because FEM models may be able to predict physical phenomena that are not actually captured by geometric shapes, this framework can potentially be used to generate more efficient and accurate plans.

Conclusions

A novel algorithm for planning optimal placement of a radiofrequency ablation needle was described. The planning method coupled FEM models, rather than geometric shapes, with an efficient search strategy to determine a needle placement that improved therapeutic outcome over a given initial placement. Simulation experiments demonstrated the feasibility of the approach in worst case scenarios when the tumor was comparable in shape to the ablation zone, and in cases where multiple ablations were required.

CHAPTER III

CHARACTERIZATION OF TRACKED RADIOFREQUENCY ABLATION IN PHANTOM

Abstract

Accurate placement of the device used to perform radiofrequency ablation (RFA) is necessary for successful therapy of solid tumors. In this work, a phantom system based on an agarose-albumin mixture was developed for evaluating optically tracked radiofrequency ablation. Calibration of the tracked probe allowed positions of distal features of the device, notably the tips of the needle electrodes, to be determined to within 1.4 ± 0.6 mm of uncertainty. Images acquired from ablation experiments performed using the tracked probe were compared to finite element models of RFA that used positional data of the RFA device obtained during ablation. The model was able to predict 90% of pixels classified as being ablated. Discrepancies between model predictions and observations were attributed to needle tracking inaccuracy as well as model parameter selection. Results suggest the feasibility of using tracked RFA as well as finite element modeling to deliver targeted ablations with predictable outcomes.

Introduction

Radiofrequency ablation (RFA) is currently a widely used treatment modality for unresectable hepatic tumors [15]. RFA produces focal therapy by delivering electrical energy directly into a cancerous lesion via needle electrodes. Because active heating is limited spatially to within a few millimeters of the RFA needle [81], the therapeutic efficacy of RFA depends on proper placement of the needle so that the final ablation extents would cover the tumor along with a suitable margin. At present, needle placement is performed using intraoperative image guidance, typically with 2D ultrasound [23]. It has been recognized, however, that guidance with 2D ultrasound can be inaccurate [36, 38]. Investigators have described various strategies of improving needle localization intraoperatively including the use of optically-based and electromagnetic[84] tracking systems to determine the location of the device relative to the targeted lesion. Various intraoperative imaging methods have also been reported including CT [37], and 3D ultrasound [39].

Although guidance provides a means of delivering the needle device to an intended destination, it depends on having a preplanned needle placement which achieves the desired therapeutic goal. Consequently, the success of therapy depends also on planning with a predictive model of RF ablations. Presently, geometric shapes using spheres and ellipses have been employed to model ablations [34]. Geometric models provide a method for rapid planning of optimal trajectories, subject to constraints placed by the anatomy of the patient[70]. Nevertheless, geometric shapes are not sensitive to the actual physical parameters that govern ablations. More sophisticated models have been studied that attempt to solve constitutive equations describing thermal ablations [53, 73]. Use of these models to develop treatment plans, however, has not been explored, especially with respect to planning placement of the RFA device.

This paper will study the problem of coupling positional information of a tracked RFA device with a computational model that predicts therapeutic outcome from physical principles that govern RFA. The goal is to characterize the spatial extents of actual ablations performed with tracked RFA in comparison to model predictions using the positional data from the tracking. To achieve this goal, several pieces of technology, which until now investigators have studied independently, will be integrated together. First a tracked RFA device will be constructed and characterized for use in locating the functional components of the device within the coordinate frame of the treatment region. Then a phantom system will be developed to help visualize the ablation outcomes performed using the tracked RFA needle. Finally, the phantom system will be imaged, and the ablation extents will be compared with finite element models of RFA solved using the measured needle positions as inputs.

Materials and Methods

Tracked RFA

Needle holder design

The ablation device used in this study was a RITA Starburst XL model radiofrequency ablation probe (RITA Medical Systems, CA). In order to track the device in space, a rigid needle holder was constructed. The needle holder served two primary functions. First, the holder reduced the bending of the RFA needle shaft so that during placement the needle shaft could be assumed to lie on a straight line. Second, the holder provided a surface for infrared emitting diodes (IREDs) to be attached rigidly at places close to the distal tip of the device where the electrodes are deployed. By localizing IREDS in space using an optical tracking system (Optotrak 3020, Northern Digital, Inc.),

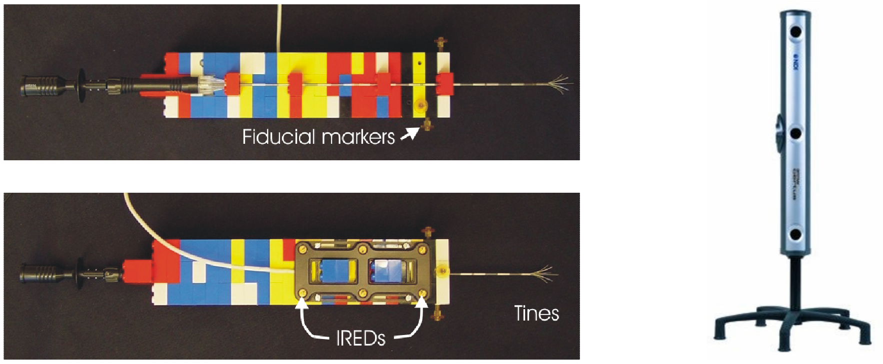

Figure III-1: (l*eft*) Pictures of the needle holder designed to track the RFA device. (*right*) Optical tracking camera similar to the one used to localize the IREDs on the needle holder (image from http://www.ndigital.com). Image dimensions are not to scale.

real time information about the location of the needle holder, and thus the needle itself, were determined.

<u>Needle holder calibration</u>

The calibration of the needle's physical location relative to the IREDs on the needle holder was achieved in two steps. In the first step, the needle axis was determined with respect to the IREDs on the holder. As shown in Figure III-1, the needle holder was constructed with a planar base so that it could be translated freely on top of a flat surface. Needle holes of the same diameter as the needle were drilled perpendicular to this base. A similar sized pivot hole was then drilled through an acrylic block on top of which the calibration experiments would be performed. While spinning the needle holder around the shaft of a needle that had been inserted through both the needle holder and the pivot hole, multiple measurements of the IRED positions were acquired. An average axis of rotation was calculated and this axis was used to define the local coordinate system of the needle holder. In particular, the axis of rotation was presumed to align with the shaft of the needle, and was set to the *z*-axis.

The second step in the calibration involved determining a fixed origin on the needle axis. In order to proceed, an arbitrary origin was initially selected along the calibrated needle axis. Using Optotrak, the transformed position of this origin was tracked as the needle holder was translated about the acrylic platform. Then, a second previously calibrated and tracked stylus instrument was used to measure the same surface by sweeping the tip of the instrument over the surface. Because both surfaces were measured in the reference frame of Optotrak, the distance between the two planar set of points was used to offset the initial point of origin along the needle axis.

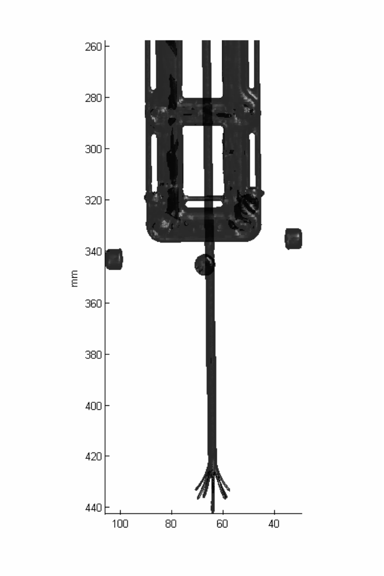

Figure III-2: Rendering of segmented CT image of RFA device attached to the needle holder, showing the deployed tines. The floating objects are the Acustar markers, while the H-shaped object near the top of the image is the frame that houses the IREDs.

Tine coregistration

A CT image of the RFA device while attached to the needle holder was acquired with the tines deployed at the manufacturer's “2 cm” setting. The locations of the 9 tine tips on the device were manually segmented and their positions in the image were recorded. Four Acustar fiducial markers [85]attached to the needle holder (see Figure III-1 and Figure III-2) were also segmented, and their centroids were coregistered with Optotrak measurements of the corresponding points. The coregistration step provided a means of transforming objects in the space defined by the Acustar markers to the space defined by the IREDs.

Needle tracking experiment

To characterize the ability of the needle holder apparatus to track the tip of a needle, experiments were performed using a hollow bore, 16 gauge needle (Popper and Sons, NY) as a proxy for the RFA device. The needle was attached to the tracked needle holder and inserted into various locations within a rigid PVC box. On the surface of the box were placed four Acustar fiducial markers. The box was filled with a 3% gelatin solution (275 Bloom, Type A, Vyse Gelatin Co., IL) to provide a solid medium into which the needle is inserted. With each needle placement, the position of the needle holder as measured by Optotrak was recorded, and then about 1 mL of a barium sulfate suspension (Lafayette Pharmaceuticals, IN) was injected into the gelatin. The barium provided a record of where the needle was placed in the box when imaged by CT. A total of 86 needle placements were recorded. The average distance from the needle tip to the origin of the needle holder was 9 cm.

In order to locate the needle tip within the CT image of the gelatin, a series of rigid transformations were computed to convert measurements in Optotrak coordinate system to the local coordinate system of the PVC box:

$$T_{needle \to PVC} = T_{needle \to holder} T_{holder \to opto} T_{opto \to PVC} \tag{3.1}$$

The transformation $T_{needle \to holder}$ was determined in the previous section; $T_{holder \to opto}$ was reported by the Optotrak system after each needle insertion into the gelatin phantom; and

$T_{opto \rightarrow PVC}$ was constructed by coregistering the physical locations and the CT segmentations of the Acustar markers, in the same manner as described in the tine coregistration step above.

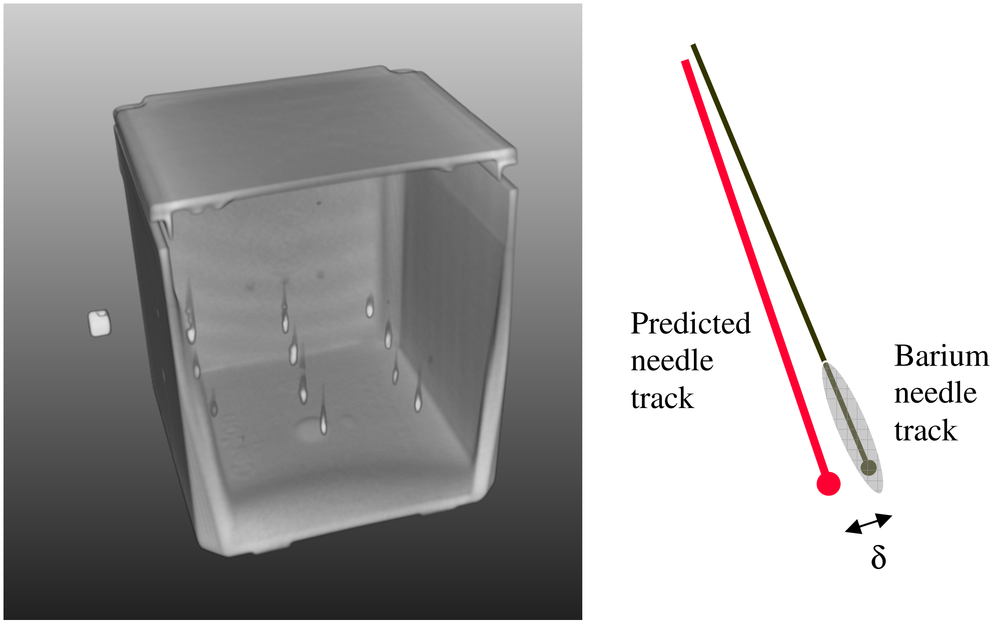

Figure III-3: (*left*) Rendering of barium tracks imaged in CT. An acustar marker is shown on the left. (*right*) Schematic showing between needle tip location predicted by Optotrak measurements, and the needle track segmented in the CT image.

Segmenting the barium tracks proceeded with the following thresholding scheme. For each barium track, pixel values greater than 1300 Hounsfield units were identified. Using the Optotrak measurement as a guide, the search was constrained to a trajectory-aligned cylindrical neighborhood around the needle tip location. The cylinder was set to be 3 mm in diameter. All other pixels were discarded. The needle trajectory was then corrected by pivoting about the measured origin of the needle holder until the average weighted distance from each pixel to the trajectory was minimized. The distance was weighted by the pixel intensities so that the trajectory would preferentially fit the higher intensity pixels produced by the concentrated barium suspension. Finally, a tip location was selected by searching the most distal pixel within a 1 mm diameter of the trajectory.

Phantom experiments

Ablations

Ablations were performed in a rectangular acrylic box (4 in. x 3 in. x 4.5 in.), designed with needle holes on the top surface (see Figure III-4). The needle holes were placed along the midline of the box. These holes served both as physical markers to collocalize with the model in subsequent analysis, and needle guides for controlled placement. This coregistration produced a transformation that mapped the coordinates from the Optotrak to the local coordinates of the phantom: $T_{opto->phantom}$.

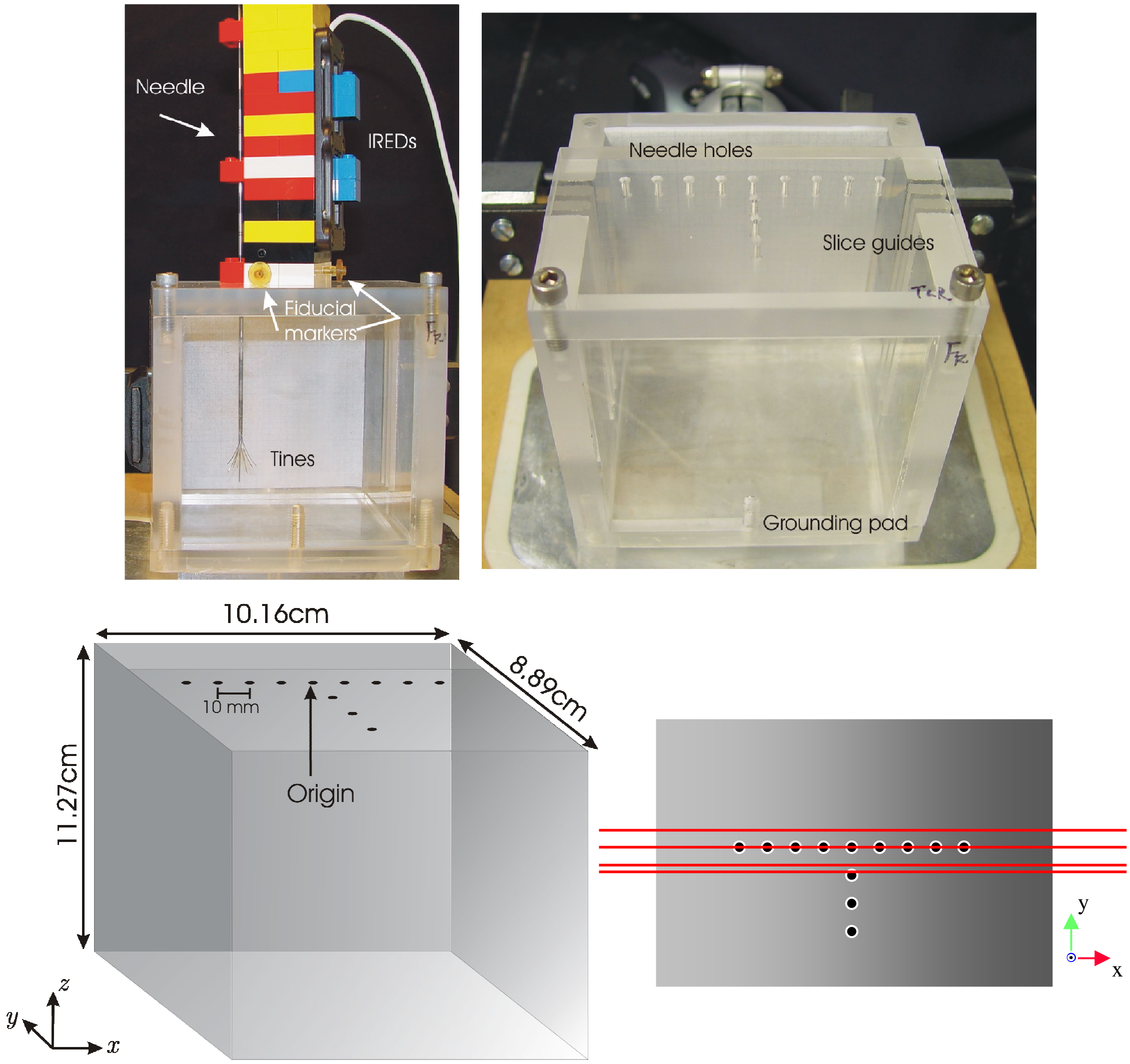

Figure III-4: (*top left*)Photograph of the phantom housing along with the needle holder and the RFA device in a setup representative of the ablation experiments. (*top right*) A close up of the phantom housing showing the needle holes, the slice guides used to aid in cutting the phantom, and the location of the grounding pad. (*bottom left*)Schematic showing inner dimensions of the phantom housing and itslocal coordinate systems. The phantom material is filled from the bottom up to an approximate height of 6.5cm. (bottom *right*)Top-down view of the phantom housing. The dark circles represent the needle holes. The dark lines show the location of the slice planes. From top to bottom, these planes are y = 5, 0, -7, and -9 mm.

The box was filled with approximately 600 ml of a tissue-mimicking agarose-albumin gel adapted from[86]. The gel was composed of agarose (1% w/v) mixed in with liquid egg white (Country Creek Farms, AR). According to the manufacturer, a 450 mL product contained roughly 50 g of proteins, of which albumin is presumably a large component. In making these gels, the agarose solution was prepared initially at a higher concentration and cooled to approximately 50 °C. The egg white solution was warmed to approximately 45 °C, before mixing in the agarose. This step prevented the albumin from being prematurely denatured by the warmer agarose solution, but also allowed the agarose solution to remain above its gelling temperature. The entire solution was then refrigerated for at least 6 hours.

Two ablations were performed each with constant power settings at 20 W for 10 minute using a RITA 500 RF generator and the RITA ablation device. Temperature measurements of the tines were manually recorded at approximately 15 second intervals. The first ablation (designated “Case 1”, in the remainder of this document) was performed with an initial background temperature of 23°C and an impedance of 26 Ω, as reported by the RITA RF generator. The device was placed through the second needle hold to the left of the center needle hole, as shown in Figure III-4. The second ablation (“Case 2”) was performed at 27°C, also with an impedance of 26 Ω. This ablation was performed in the same phantom as in Case 1, but occurred after 1 hour of cooling time to allow the phantom material to return to baseline temperatures. The device was placed obliquely into the ablation to approximately the same depth as the first ablation.

Photogrammetry

After ablations were performed, the agarose-albumin block was sectioned manually with parallel cuts located at the planes shown in Figure III-4. These sections were then photographed digitally into images of 1280x960 resolution. The resulting images were rescaled so that the width of the imaged phantom corresponds to the inner diameter of the phantom housing. Finally, the images were realigned so that the edges of the phantom in each image match.

Computational Model

A finite element model was developed for the phantom system in order to determine if the ablation results could be predicted by computational modeling. In particular, the model would be used to test if the the ablation extents align in space with images of the ablation outcome.

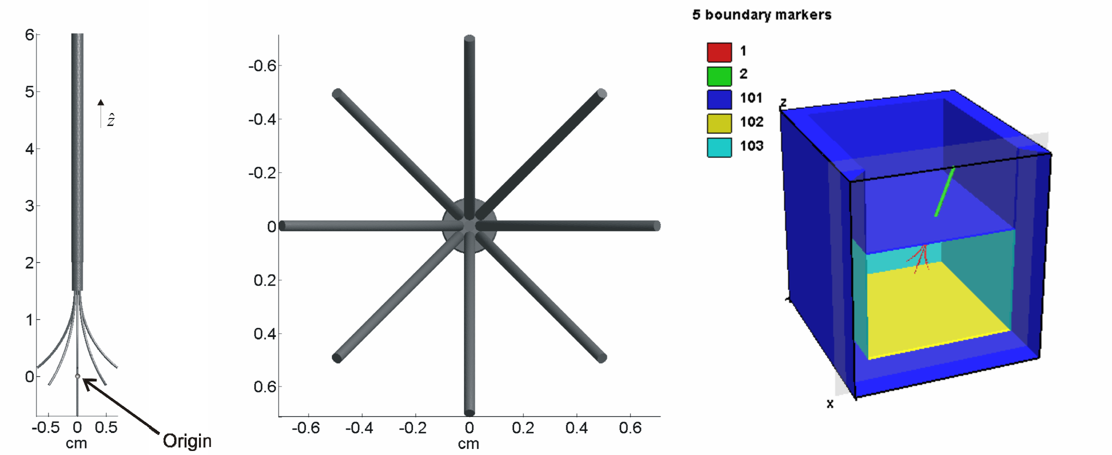

Figure III-5: (*left*)The surface model of a commercially used ablation device, along with its local coordinate system. (*middle*)A close up of the tine arrangement from the bottom. (*right*)A surface mesh of the phantom geometry with a needle penetrating the phantom surface.

Model geometries

Shown in Figure III-5 is the surface mesh of the domain geometry and the needle model. The model was constructed to mimic the dimensions of the acrylic box.

Excluding the RFA device, two material domains were used: one representing the acrylic box, and the other the phantom material. The top surface of the phantom material was set so that the total volume would be 600 mL.

The needle geometry was then placed according to the orientation and position provided by Optotrak. To achieve this goal required the coregistraton of the needle geometry to the CT image of the physical device. First the shaft of the needle was aligned with the segmented shaft of the CT. Then, the tines of the needle geometry were coregistered with the tine measurements obtained earlier, producing the transformation $T_{RFA \rightarrow holder}$. It should be noted that in the last step, the registration was constrained only to rotation about the shaft as well as translation along the shaft. As in (3.1), the total transformation from the local coordinates of the RFA device to the coordinates of the phantom is then given by a series of transformations:

$$T_{RFA \rightarrow phantom} = T_{RFA \rightarrow holder} T_{holder \rightarrow opto} T_{opto \rightarrow phantom} \tag{3.2}$$

A mesh was then generated using a freely available meshing software package, Tetgen [72]. Special modifications were made to this software to allow repair of intersecting surfaces caused, in particular, by the insertion of the needle geometry through the surface of the phantom material.

Constitutive equations

Computational models of thermal ablation start with a thermal diffusion model:

$$\rho c \frac{\partial T}{\partial t} = \nabla \cdot k \nabla T + Q_{RF} \, , \tag{3.3}$$

where Q_{RF} (W/cm^3) is the heat source due to RF currents, and T (°C) is the temperature. All other material coefficients are defined in Table III-1. The heat source, Q_{RF} can be approximated by first solving the electrostatic problem with appropriate boundary conditions:

$$-\nabla \cdot \sigma \nabla \Phi = 0, \tag{3.4}$$

where σ (S/cm) is the conductivity of the medium, and Φ(V) is the electrostatic potential. Given Φ, the heat source is then estimated as the time-averaged power density generated by the resulting current: $Q_{RF} = \left(P_{set} / P_0 \right) \frac{1}{2} \sigma \left| \nabla \Phi \right|^2 \eta$, where P_0 is the input power resulting from 1.0 V being applied to the needle, and P_{set} is the actual power setting, which is 20.0 W. The parameter η represents a phenomenological term that is used to account for unknown power losses due to inaccurate parameter selection and potential discrepancy in the power level reported by the RF generator. This parameter was titrated using 1% increments starting from 100%, until the temperature distributions matched the predicted ablation in a control experiment. This value has been set to 90% for all simulations.

Boundary conditions are specified as follows. For the electrostatic problem, the outer surface except the bottom face is prescribed an insulative, no flux condition. A constant 1.0 volt Dirichlet condition is applied on the conductive electrodes, and ground is placed on the bottom face. The total power P_{set} was set to 20 W, and the entire ablation was run for 10 minutes, after which the power was set to 0 W.

Table III-1: List of material properties used in RFA simulation. Values represent the initial properties used in the simulations. As simulations proceed, the temperature-dependent properties change.

Properties	**Symbol (units)**	**Value**
Thermal diffusivity (phantom)	k (W/cm·K)	5.72e-3
Density (phantom)	ρ (g/mL)	1.03
Heat capacity (phantom)	c (J/g·K)	3.94
Electrical conductivity (phantom)	σ (mS/cm)	4.4
Activation energy	ΔE_a (J)	3.846e5
Activation factor	A (s^{-1})	3.75e57
Thermal diffusivity (acrylic)	k (W/cm·K)	1.7e-3
Density (acrylic)	ρ (g/mL)	1.19
Heat capacity (acrylic)	c (J/g·K)	1.4
Electrical conductivity (acrylic)	σ (mS/cm)	1e-14

Finally, a measure of accumulated protein denaturation over the course of the ablation is computed. A suitable metric is the Arrhenius damage index, which has been previously employed by investigators to model optical changes in albumin upon heating [86]. It is given by:

$$\frac{\partial \omega(\mathbf{x},t)}{\partial t} = -A \exp\left(-\frac{\Delta E_a}{RT(\mathbf{x},t)}\right)\omega(\mathbf{x},t), \qquad (3.5)$$

with the initial condition that $\omega(\mathbf{x},t_0)=1$. The Arrhenius survival function, ω, can be interpreted as the ratio of undenatured proteins to total proteins within a given region of space. Thus in the case of the phantom, $\omega = 1$ corresponds to albumin in its native state, whereas $\omega << 1$ indicates the albumin is denatured. In this work, the threshold used to demarcate the denatured coagulum was set to $\omega_0 = e^{-1}$ or approximately 37%.

Material properties

As suggested previously by other investigators [53, 55], this model implemented temperature dependent electrical conductivity. In particular, the electrical conductivity of ionic solutions, notably that of the phantom material, increases at a rate of 2%/°C [77]. The temperature dependence of other parameters were not modeled because their inclusion in the model would produce relatively small changes in the final temperature [79]. As the mesh was regenerated for each needle placement, routines are implemented to assign appropriate material properties to each tetrahedral element.

A method for estimating the thermal properties was proposed in [86] based on the estimated water content of the material by mass, and adopted in this study. The water content of the phantom was estimated based on the protein content (albumin) and agarose (56 g) as compared to the total mass of the gel (600 g), resulting in a ratio of 93%. The electrical conductivity of the phantom was estimated to be 4.4 mS/cm at 23 °C based upon the impedance reported by the generator, and using the assumption that the material was homogeneous. Finally, the Arrhenius parameters were those used in [86].

Iterative solver

In order to solve the coupled equations, the finite element method (FEM) [53, 56, 73, 74] was used to discretize the problem spatially. An external iterative solver package (PETSc, [80]) was used to obtain the solution of the resulting systems of equations using an iterative scheme. The transient temperature solution was computed over 15 minutes via a fully implicit time-stepping scheme, at intervals of 15 seconds. Temperature-dependent properties were updated by using the temperature distribution from the previous iteration. A constant power setting was imposed on the electrostatic problem by scaling the total power in the domain to 20.0 W at every time step. After 10 minutes of ablation, the applied power was set to zero. All algorithms were implemented in C++ on a Win32 platform using a Pentium 3.4 GHz processor with 2 GB of RAM. For further details on the implementation, please see Chapter II.

Model accuracy

In order to evaluate the accuracy of the model two parameters were developed based on the pixels from the imaging studies of the phantom results. The *sensitivity*, S, measures the ratio of the number of ablated pixels which coincide with the model, N_{overlap}, to the total number of segmented pixels, N_{observed}: $S = N_{\text{overlap}} / N_{\text{observed}}$. The *positive predictive value*, P, measures the ratio of the overlap of ablated pixels with the model to the total number of pixels inside the model, $N_{\text{predicted}}$: $P = N_{\text{overlap}} / N_{\text{predicted}}$. As an illustration, a large sphere that covers the entire region of interest would result in a S value of 1, but at the cost of a low P. At the other extreme, a model that predicts a tiny spherical ablation in the middle of the observed ablation pixels would have a high P but a low S. It is desirable to have high S and P values because it implies the model would be able to predict the observed ablation results with high probability without the model's being overly permissive in predicting ablated pixels.

In anticipation of needle tracking inaccuracies, a method was used to test whether the model accuracy would improve only by changing the position of the needle, while other model parameters remained the same. Using an image processing technique previously described (see Chapter II), the RFA needle was repositioned from the measured placement with the objective of overlapping more of the observed pixels. In addition, the model results were compared to spherical geometries commonly used in the ablation literature to model ablations.

Results

Needle tracking experiments

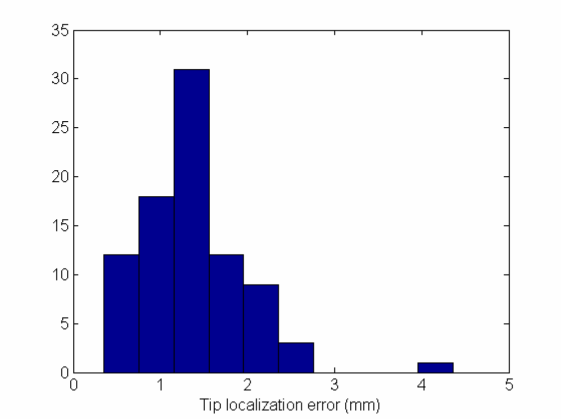

Figure III-6: Histogram of the distance between needle tip location predicted by Optotrak and as observed in CT imaging.

The average needle placement error was 1.4 ± 0.6 mm, and the figure above shows the calculated error distributions. This result is comparable to a previous study using a similar barium track technique for evaluating needle tip tracking in gene therapy application [87]. One source of uncertainty in this experiment is the distribution of barium within the needle track. Because gelatin tends to crack upon applied stress, the barium tracks may have extended further than the true needle tip position. Indeed, if the needle length is considered fixed, then expected tip location as projected from the tracked origin of the needle holder is consistently shorter than the tip location estimated from the CT image. On average, this biased extension along the needle is approximately 0.8mm.

Phantom experiments

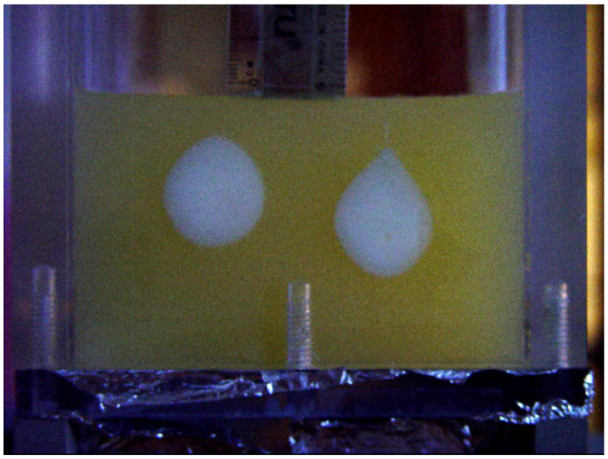

Figure III-7: Ablation outcome for the slice at y = 0mm.

Needle coregistration

The registration error in $T_{RFA \rightarrow holder}$ used to map the tine tips of the physical needle to the needle geometry used in FEM modeling was 0.88 mm. This result reflects discrepancies between the symmetric arrangement of the tines used in modeling compared with the actual asymmetries in the physical device. Ideally, the geometry should match that of the physical device since electrical power is concentrated in the tine tips, and thus, accurate localization of the tine tips could potentially produce more accurate modeling. Nevertheless this result is reasonable given the inherent difficulty in localizing flexible mechanical systems such as the tines in the RFA device.

Temperature traces

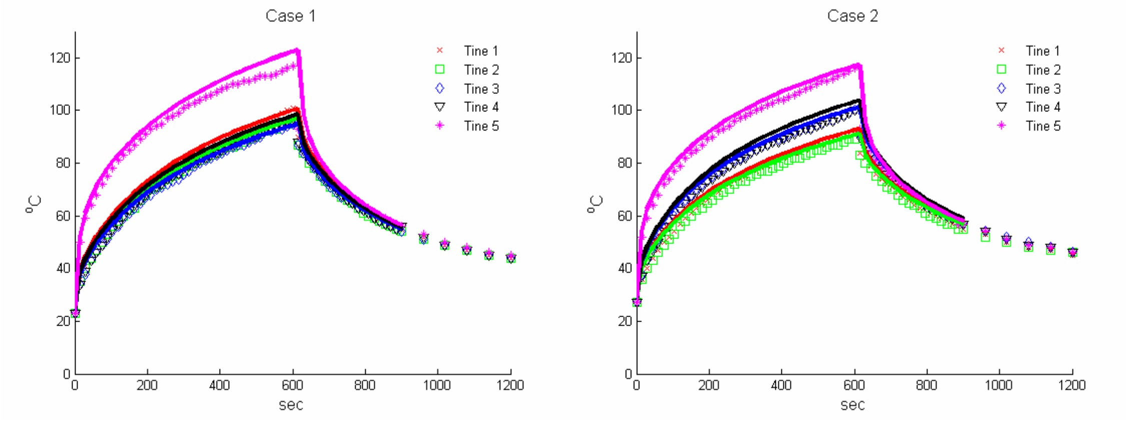

Figure III-8: Temperature traces from (*left*) case 1 and (*right*) case 2. The marked points are the recorded temperatures provided by the RFA system. The solid lines represent the model predictions

The RITA RF system contains thermocouples embedded in the outer tines, and during the ablation experiments, these measurements were recorded manually. The tines have been labeled to match the scheme used by RITA, in which tine 1 is the center tine, and tines 2 through 5 are the outermost tines, corresponding to the tines placed on the cardinal axes shown in Figure III-5. As graphed in Figure III-8, the temperature measurements agreed with the model predictions well. At higher temperatures, however, there is some deviation with the model, particularly visible in the plot for case 1. This discrepancy is likely the result of additional dynamics, such as vaporization of water, or the desiccation of the phantom resulting in decreased power delivery locally. The FEM model does not currently include these dynamics. In both placements tine 1 is closest to ground, and hence is the path of least resistance for the RF current. Thus, more power is preferentially deposited there. Also of note is that even though the remaining 4 tines are arranged symmetrically about the axis of the device, there is some difference between the temperature distributions. This difference is most noticeable in case 2, in which the tines are placed at different distances from ground because of the oblique angle of insertion. The most straightforward explanation of these differences in local temperature is that they are the results of boundary effects.

Image analysis

The imaged ablation outcomes were segmented using a thresholding scheme. The processed image corresponding to the slice plane $y = 0$ mm, as displayed in Figure III-7, is updated in Figure III-9. The measured needle placements were generally in the right vicinity of the corresponding ablation for each case. Furthermore the modeled ablations agreed with the imaged ablations. The next sections provide quantification of this agreement.

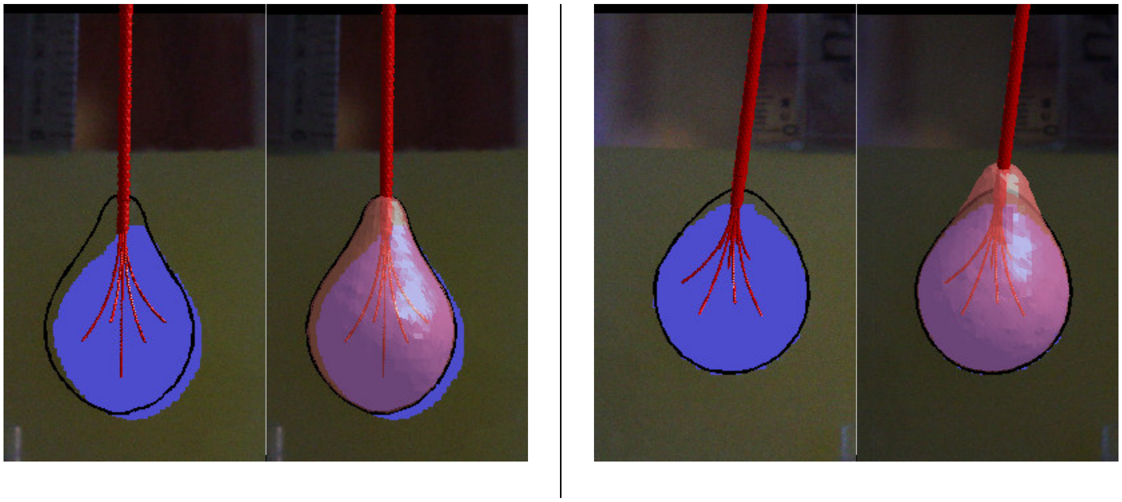

Figure III-9: Ablations at slice y=0 mm for (*left pair*) case 1 and (*right pair*) case 2. The dark mask represents the segmented pixels corresponding to the ablated albumin. The surfaces provide a three dimensional context of the overall ablation shapes. The intersection of the surface with the plane is given by the black outline.

Model accuracy

The results presented in the table demonstrate that with the raw measurements of needle position, the model is capable of predicting at least 90% of the pixels that had been classified as being ablated. In achieving this result, however, the model predicted roughly 17-19% more pixels (*i.e.* from calculating the ratio of *S* to *P*) as ablated than than were classified as being ablated. The overestimation of the ablation extents is likely a result of inaccurate model parameters. On the other hand, the differences in S values between the two cases may be perhaps better explained by inaccurate needle tracking.

Table III-2: Table of parameters characterizing model accuracy. The bottom row lists the maximum displacement of a tine in the repositioning process.

	Case 1		**Case 2**	
	Original	Repos'd	Original	Repos'd
S_{FEM}	91.6%	99.1%	99.4%	99.9%
P_{FEM}	77.9%	82.6%	83.7%	81.8%
S_{sphere}	--	81.5%	--	71.3%
P_{sphere}	--	100%	--	100%
Max tine shift	1.4 mm		1.7 mm	

Needle repositioning

Table III-2 lists the results from repositioning the needle in model simulations in an attempt to increase model overlap with observed pixels. In both cases, the *S* values increased, an expected result since the goal was to increase the numerator of *S*. In particular, with case 1, the data suggests that the needle tracking error was a major contributor to the reported inaccuracies as both *S* and *P* increased while the ratio of *S* to *P* slightly increased from 18% to 19%, suggesting that the modeled ablation could capture more pixels simply by reposition rather than by increasing its size. In case 2, however,

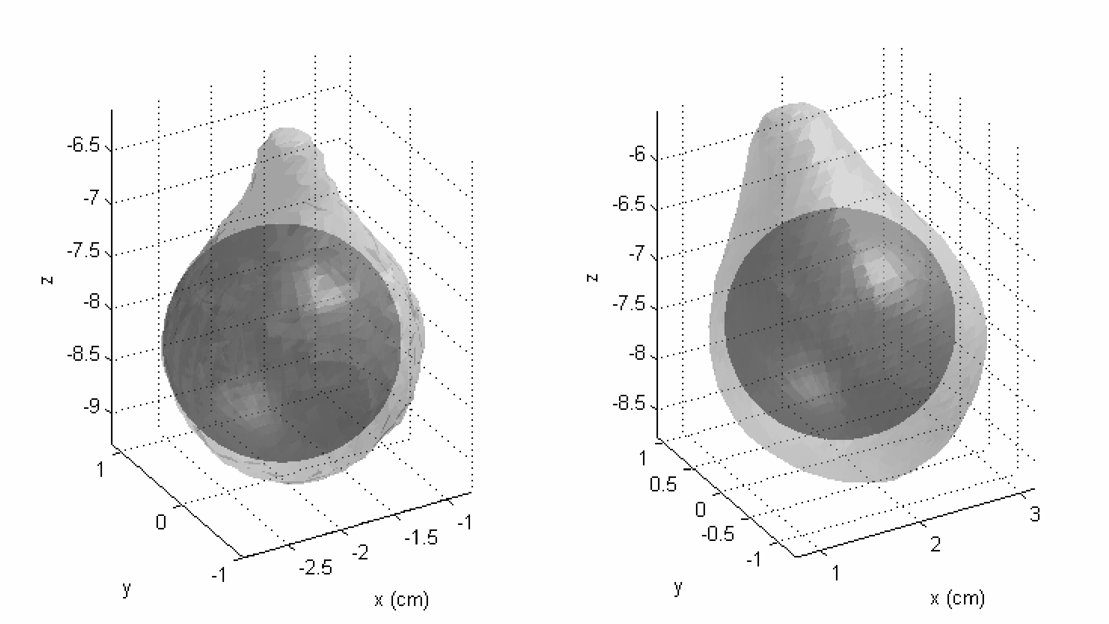

Figure III-10: The diagram shows, in the coordinate system of the phantom, the largest spheres that fit the ablated pixels, with the corresponding FEM prediction overlaid. (*left*) Case 1. (*right*) Case 2

there was a marginal increase in S while P decreased. This result indicated that the algorithm positioned the needle in a manner that produced a larger ablation in order to overlap more ablated pixels. Nevertheless the decrease in P was marginal, and the fact that both cases had roughly the same value of P suggests that some shared parameters used in modeling the ablations were likely affecting the overestimation of the ablation size. These parameters may include discrepancies between true and simulated material properties, or the incorrect choice of threshold, ω_0. This latter prospect is further explored below. It is of note that if the repositioned needle represents the true location of the physical device, then the amount of displacement of the tines is comparable to the error reported in the needle tracking experiment above.

Comparison with sphere fits

The results obtained with the repositioned FEM models were compared with spherical ablation geometries. Each of the corrected ablation zones was fit with the largest sphere that was entirely contained within the observed pixels. The results are shown in Figure III-10. As can be seen, the sphere fits the fatter portion of the teardrop-shaped ablation, but fails to account for the narrower portion near the shaft of the device. This observation is further illustrated in Figure III-11, in which the model accuracy was quantified using the S and P values described earlier. For the repositioned FEM model, these curves were created by varying the treshold Arrhenius survival fraction. For the sphere model, they were generated by varying the radius of the fitted spheres. In general, in order to achieve an S value that is greater than 90%, the graphs show that the FEM model were able to do so at a higher P than using the sphere model. In other words, if both model were fitted to capture 90% of the observed ablated pixels, the sphere model would cover more nonablated pixels than the FEM model. Although these results may seem to favor FEM only slightly, it is worth mentioning that these phantoms do not include the effects of vasculature. In those circumstances, FEM model may outperform spherical models more significantly because geometric models do not account for heat sink effects. It remains to be seen if methods proposed in [10], may enhance predictivity of geometric models.

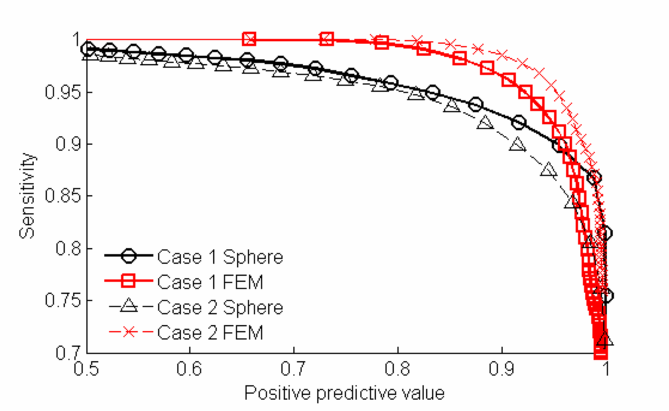

Figure III-11: Receiver operator characteristics of sensitivity, *S*, and positive predictive value, *P*, values using sphere and FEM ablation models for each of the two ablation results. The curve was generated for the FEM model by varying the contour threshold, whereas for the sphere model, the sphere radius was varied.

Conclusions

In this paper, evidence was presented to support the use of tracked RFA device in producing ablations whose spatial extents are predictable by computational modeling. Needle placement experiments demonstrated the ability of the optical tracking system to localize functional features of the device, particularly the electrodes, in space. Ablations were performed inside a phantom system with the tracked device, and the positional data of the device were used in computational models of the ablation. Results from the simulations demonstrated the feasibility of the models in predicting at least 90% of the ablated pixels in images of the phantom.

CHAPTER IV

SENSITIVITY ANALYSIS OF NEEDLE PLACEMENT IN RADIOFREQUENCY ABLATION PLANNING USING A BEM-FEM APPROACH

Abstract

A computational method is presented for optimizing needle placement in radiofrequency ablation treatment planning. The parameterized search is guided by an objective function that depends on transient, finite element solutions of coupled thermal and potential equations for each needle placement. A framework is introduced for solving the electrostatic equation by using boundary elements to model the needle as discrete current sources embedded within a finite element mesh. This method permits finite element solutions for multiple needle placements without remeshing. We demonstrate that the method produces a search space amenable to gradient-based optimization techniques. The method is then used to analyze the sensitivity of the optimized needle placement to random perturbations in its position by means of Monte Carlo simulations. The results of the sensitivity analysis demonstrate that localization errors decrease the effective ablation extent inside the treatment region. Information from this analysis may be incorporated into clinical planning strategies.

Introduction

Radiofrequency ablation (RFA) is used increasingly as a thermal ablative modality for treating unresectable liver tumors. Needle electrodes deployed inside the tumor generate RF currents that result in the thermal destruction of malignant tissue with minimal side-effects. Nevertheless, success of RFA has been limited when treating tumors that are larger than 3 cm in diameter [28]. Computational models have become integral in understanding the roles that thermal and electrical characteristics of the liver [53] play in RFA treatment. In addition, computational models that predict proper placement of the RFA needle have become the focus of significant research, particularly with regards to application of image-guided techniques [34]. In treatment planning of RFA, an important goal is the identification of suitable needle placements within the treatment region such that the therapeutic outcomes, as predicted by a model of RFA, are maximized. Another goal is to take into account possible misplacement of the needle during implementation of the plan. These localization errors in targeting a predetermined location within an organ are caused in large part by mechanical deformation of the organ [88], organ motion due to respiration [84], as well as intrinsic tracking errors in the surgical navigation system [43].

Currently, models of RFA used in needle placement or trajectory planning typically assume that the resulting spatial extents are geometrically spheroid or ellipsoid. The goal in geometric planning is to arrange copies of these fixed shapes so that together they would cover a tumor along with a 1 cm margin [46]. It has been recognized, however, that geometric models of ablation may not be sufficiently predictive in situations where thermal sinks, produced by large blood vessels that remain patent during ablation, are close to the treatment area [31]. On the other hand, computational models, solved in particular by finite element methods (FEMs), are capable of producing predictive results based on physical laws that govern ablation [53, 55, 73]. Nevertheless, little has been reported on how to incorporate FEM based solutions into treatment planning.

An obstacle to using FEM models for treatment planning is that significant computational effort may be required to evaluate ablation outcomes from different needle placements. One such burden is in preprocessing the model geometries in order to discretize the problem into a manageable system of equations. In a straightforward implementation, a mesh would have to be regenerated for each new needle placement before the model can be solved. Mesh generation, however, is indirectly a computationally expensive process, especially in meshes containing geometrical features that vary significantly in characteristic length scales. In particular, with respect to RFA modeling, the diameter of the tines of the probe is typically much smaller than other objects, and thus requires much refinement during mesh generation. This refinement causes solvers of the FEM models to expend disproportionate computational effort on solving variables in a relatively small region of space compared to the treatment volume. Another source of computational burden lies in the postprocessing steps that are required to compare solutions from different needle placements. Depending on the meshing technique, meshes may differ significantly from even slight perturbations to needle orientation and position. Thus, in order to compare results from remeshed solutions, additional interpolation steps need to be taken, for instance, by sampling irregularly spaced FEM solutions onto a regular Cartesian grid.

For these reasons, a method will be presented in this paper that eliminates the need for remeshing and allows solutions of linear FEM models for varying needle positions to be solved efficiently. The method uses a current-source representation of the needle electrodes as opposed to a constant voltage representation. The novelty in the approach is that the current source may be coupled into FEM with a fixed mesh by means of direct integration. The current source distribution is solved using the boundary element method, which discretizes the electrostatic problem into a smaller, albeit more dense, system of equations than FEMs. After describing the method, it will be coupled with an optimization routine to search various needle placements in a given domain. Then, the method will be integrated into a Monte Carlo simulation to study the sensitivity of the optimized placement to perturbations to its position in order to model effects of needle localization inaccuracies encountered in real world RFA applications.

Methods

Computational models of thermal ablation usually begin with Pennes bioheat equation to solve for the thermal distribution as a result of a local heat source:

$$\rho c \frac{\partial T}{\partial t} = \nabla \cdot k \nabla T - h_b \left(T - T_a \right) + Q_{RF} , \tag{4.1}$$

where Q_{RF} is the heat source due to the radiofrequency current, T is the temperature, and explanations of other coefficients may be found in [73]. In radiofrequency ablation, Q_{RF} can be approximated by first solving the electrostatic problem with appropriate boundary conditions:

$$\text{-}\nabla \cdot \sigma \nabla \Phi = 0 \tag{4.2}$$

where σ is the conductivity of the medium, and Φ is the electrical potential. Given Φ, the heat source is then estimated as the time-averaged power density generated by the resulting current: $Q_{RF} = \frac{1}{2}\sigma\left|\nabla\Phi\right|^2$. In order to solve the coupled equations, most investigators have employed the finite element method (FEM). FEM models for radiofrequency ablation typically solve the electrostatic problem over a single meshed domain, Ω, that is shared with the thermal problem. As a matter of convenience, a single mesh shared for both equations allows the estimated power deposition from the electrostatic equation to be input directly into the FEM formulation of the thermal problem without additional interpolation steps.

Current source representation

The technique developed to minimize remeshing exploits a well-known duality in electrostatics and circuit analysis regarding voltage sources and current sources. Specifically, for a voltage distribution that results from applying a constant voltage source to the needle (*i.e.* a Dirichlet boundary condition), there is an equivalent current source distribution (*i.e.* a Neumann boundary condition) that will generate the same voltage distribution in the domain. The advantage of this equivalence is that a current source can be handled in FEM techniques independently of the mesh. The disadvantage is that the magnitude of the equivalent current source that would result in the correct voltage distribution is unknown. In order to provide an approximation to the current source strength, another technique – the boundary element method (BEM) – is utilized. In order to simplify the development of the method, the following additional conditions are imposed. The constitutive models described in equations (1) and (2) will be linear with spatially homogeneous properties and solved in 2D domains. In the electrostatic problem, the ablation needle itself is represented as a 1D shell (*i.e.* a linear curve) within the domain, Ω, while the inactive portions of the needle such as the shaft of the needle are not modeled. In the electrostatic problem this latter approximation is acceptable, since the nonconductive needle shaft does not affect the current magnitude significantly. The needle is assumed to be a perfect conductor, and thus Dirichlet boundary conditions for the potential problem are prescribed on the needle. In the thermal problem, the needle itself is assumed not to have a material effect on the temperature distribution beyond acting as a heat source.

To help illustrate the methods, the prototype problem shown in Figure IV-1 is used. The geometry of the prototype problem is a rectangular domain measuring 20 cm x 30 cm. For the thermal problem, the prescribed boundary condition for all edges of the rectangle is $T = 37°\text{C}$. For the potential problem, the edges are insulated (*i.e.* $\nabla\Phi \cdot \hat{n} = 0$), except for the rightmost edge which is grounded at $\Phi = 0$. The region of interest (ROI) is a circle with a diameter of 4 cm containing the needle. The needle is prescribed the boundary condition $\Phi = \Phi_0$, which is set so as to produce a predetermined power level. The blood vessel is given the fixed boundary condition $T = 37°\text{C}$.

As mentioned above, to eliminate FEM remeshing during optimization searches, BEM is employed to solve an equivalent potential problem, the solution of which is a current source distribution that can be readily coupled with a static mesh FEM. The equivalent problem is described by Poisson's equation:

$$-\nabla \cdot \sigma \nabla \Phi^B = j \tag{4.3}$$

where j is a surface current source model that is only active on the boundary of the needle[1]. For 2D problems, j is thus represented by a line source of infinitesimal width. Though the spatial distribution of j along the surface of the needle is initially unknown, the voltage distribution is constrained by the same Dirichlet boundary conditions as in the original Laplace's model.

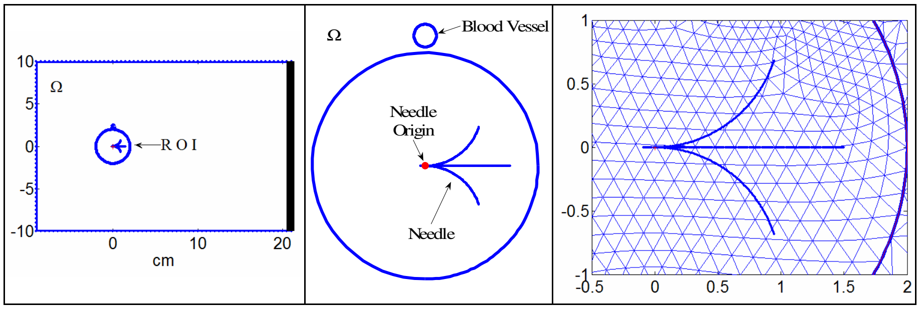

Figure IV-1: (*left*) The geometry of the prototype problem; (*middle*) the region of interest (ROI); (*right*) closeup of the ROI shows the needle source elements embedded in the triangular mesh.

BEM uses the following integral formulation of Poisson's equation:

$$\begin{aligned} c(\mathbf{x})\Phi^{BEM}(\mathbf{x}) = \int_{\partial\Omega} G(\mathbf{x},\mathbf{y})q(\mathbf{y}) - \Phi^{BEM}(\mathbf{y})\nabla G(\mathbf{x},\mathbf{y})\cdot\hat{\mathbf{n}}\,ds_{\mathbf{y}} + \\ \int_{\Omega} G(\mathbf{x},\mathbf{y})\,j(\mathbf{y})\,d\Omega_{\mathbf{y}} \end{aligned}, \qquad (4.4)$$

where $G(\mathbf{x},\mathbf{y})$ is the Green's function for potential fields in free space, q is the normal flux at a boundary, and Φ^B is the potential. For 2D potential problems, $G(\mathbf{x},\mathbf{y}) = -\frac{1}{2\pi}\log|\mathbf{x}-\mathbf{y}|$. The coefficient term, $c(\mathbf{x})$, is defined to be ½ if $\mathbf{x}$ is on a boundary, and 1 if $\mathbf{x}$ is inside the domain and located on a current source.

---

[1] In the BEM literature, this equivalence, wherein boundary conditions are treated as sources embedded in the domain, is known as an *indirect* formulation.

In order to solve this integral equation, the current source and the boundary are divided geometrically into N_s and N_b elements, respectively. The resulting discretized integral equation for each element produces a system of $N_b + N_s$ equations, which can be written in matrix notation: $\mathbf{H\Phi^B} = \mathbf{Gq} + \mathbf{Bj}$. Using the collocation method [89], the entry in row *i* and column *k* of the matrices **G** and **B** is the result of evaluating the surface integral of $G(\mathbf{x}, \mathbf{y})$ along element *k* at the collocation point on element *i*. On the other hand, the entries of the matrix **H** represent contributions from the boundary integral of $\nabla G(\mathbf{x}, \mathbf{y}) \cdot \hat{\mathbf{n}}$ along element *k* to the i^{th} element. All integrals are evaluated analytically. As written in (4.4), the vectors $\mathbf{\Phi^B}$, **q**, and **j** represent the boundary voltages, boundary fluxes, and source currents at the collocation points of the boundary elements. It should be noted that the vectors contain both unknowns and knowns. In particular, wherever an element is prescribed a Neumann condition, the corresponding component of $\mathbf{\Phi^B}$ needs to be solved. Similarly, if a Dirichlet condition is prescribed, then the corresponding component of **q** needs to be solved. All elements of **j** are unknown, and it is the object of this method to determine their values. To proceed then, the unknowns are first collected onto the left hand side. The resulting system of equations, which appears in the form $\mathbf{P\alpha} = \mathbf{b}$, is solved. The solved variables are then resorted into the original vectors $\mathbf{\Phi^B}$, **q**, and **j** to obtain the desired solutions. For further details on implementing BEM, the following text is recommended [89]. A representative BEM solution is shown in Figure IV-2.

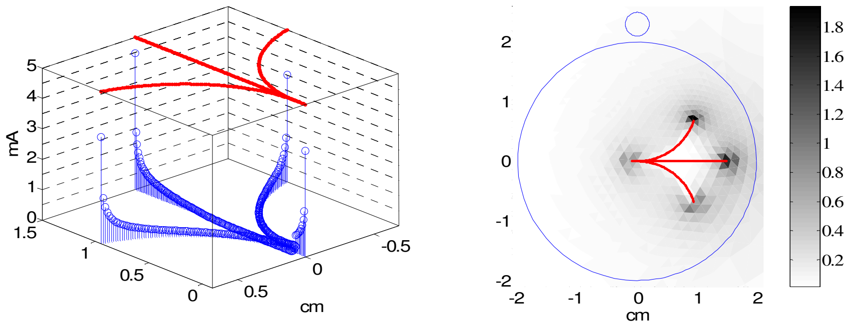

Figure IV-2: (*left*) The graph depicts a representative current distribution along the needle solved using BEM with $\Phi_0 = 163$ V and $\sigma = 1.48$ mS/cm. The resulting power density is shown for each element of the mesh (*right*).

Power Density Estimation

Once the boundary element problem is solved, an estimate for the current source model is obtained. In order to estimate the power density, the current source model is used with FEM to estimate the potential everywhere else in the domain. The standard Galerkin formulation of Poisson's equation in FEM analysis is:

$$\int_{\Omega} \sigma \nabla\Phi^F \cdot \nabla\varphi_i \, d\Omega - \int_{\partial\Omega} \varphi_i \left(\sigma \nabla\Phi^F \cdot \hat{n}\right) ds = \int_{\Omega} j\,\varphi_i \, d\Omega \qquad (4.5)$$

where $\Phi^F = \sum_{k=1}^{N_e} \Phi_k^F \varphi_k$, and φ_k is chosen to be a piecewise linear basis function. The right hand side of equation (4.5) is coupled to the BEM solution via the current source, *j*, which is composed of piecewise constant line elements. In order to evaluate this domain integral, it is therefore necessary to identify which elements in the FEM mesh contain a line element representing the current source. Two steps are required. First, point-in-triangle queries are used to identify which finite elements contain the endpoints of a boundary element. Then, the segments are partitioned amongst the finite elements by solving for the points of intersection between the boundary element and the edges of the finite element. Both computational geometry problems have been well studied [90]. As can be seen in Figure IV-1, relatively few triangular elements of the FEM mesh contain line elements of the BEM mesh, and thus, efficient data structures can be used to speed the search for triangle-line intersections. After the line sources are partitioned among the triangle elements of the FEM mesh, the source integrals in (4.5) can be evaluated via Gaussian quadrature, resulting in the following system of equations, written in matrix form: $\mathbf{K}_E\mathbf{\Phi}^{\mathbf{F}} = \mathbf{f}_E$. After the nodal values are solved, the power density for the i^{th} element is estimated by $Q_i = \frac{1}{2}\sigma\left|\nabla\Phi_i^F\right|^2$, which is constant within the element for piecewise linear basis functions.

In order to model RFA with a constant-power setting, the voltage applied to the needle, Φ_0, was scaled so that the total power deposited in Ω was equal to a prescribed level. Although other power delivery schedules like constant temperature settings are used in clinical applications, they are more difficult to simulate because of proprietary control logic designed by the manufacturers of the RFA system [91]. Nevertheless, adapting this method to time-varying power schedules should be straightforward. A typical solution of the power deposition is shown in

Figure IV-2. Given the power deposition, transient solutions to the thermal problem can be obtained via the FEM formulation of the thermal problem:

$$\rho c \int_{\Omega} \frac{\partial T}{\partial t} \varphi_k \, dt = \int_{\Omega} -k\nabla T \cdot \nabla \varphi_k + \left\{ h_b \left(T_a - T \right) + Q_k \right\} \varphi_k \, d\Omega + \int_{\partial\Omega} \varphi_k \left(k\nabla T \cdot \hat{n} \right) ds \quad , \qquad (4.6)$$

which can be rewritten in matrix notation as $\mathbf{M}_T \, \partial\mathbf{T}/\partial t = \mathbf{K}_T\mathbf{T} + \mathbf{f}_T$. Because the FEM mesh needs to be generated only once and the models are linear and coupled only via the heat source, the FEM matrices $\mathbf{K}_E$, $\mathbf{K}_T$ and $\mathbf{M}_T$ need only be computed and stored once. Thus, for each step in an optimization search, only the vectors $\mathbf{f}_\mathbf{E}$ and $\mathbf{f}_T$ need be updated.

Needle placement optimization

The Arrhenius survival function is a commonly used index for evaluating thermal ablation. The index is the solution to a first order differential equation with a temperature-dependent rate constant:

$$\frac{\partial \omega(\mathbf{x},t)}{\partial t} = -A \exp\left(-\frac{\Delta E_a}{RT\left(\mathbf{x},t\right)} \right) \omega(\mathbf{x},t) , \qquad (4.7)$$

with initial condition, $\omega\left(\mathbf{x},t_0\right) = 1$. The variable ω can be loosely interpreted in the context of thermal ablation to mean the ratio of viable cells to all cells. Other parameters in the equation are explained in [53]. After ablation, a smaller value of ω everywhere within the tumor would indicate a higher likelihood of ablation success. Thus, a suitable objective function can be defined by spatially integrating ω, evaluated at some fixed time t_f after the beginning of ablation, over the region of interest (*i.e.* the tumor):

$$\mathcal{J} = \int_{ROI} \omega\left(\mathbf{x}, t_f\right) d\Omega . \tag{4.8}$$

For each time step in solving the transient temperature distribution, ω is updated at each node of the finite element mesh. The same basis functions used in solving the FEM problems are applied to interpolate the nodal values of ω. Finally, quadrature can be performed over each element of the mesh that belongs in the ROI.

Because the transient temperature distribution is a function of the heat source, the objective function in (4.8) is implicitly a function of the position of the 2D needle. Consequently, the objective function can be parameterized by three degrees of freedom describing a rigid transformation of the needle: the x and y positions, and a rotation ϕ about the origin of the needle. If $\boldsymbol{\theta}$ is defined to be the vector of these three degrees of freedom, then the optimization problem searches for $\boldsymbol{\theta}$ that minimizes $\mathcal{J}(\boldsymbol{\theta})$. The search method employed is an unconstrained steepest descent algorithm [82]. The gradient of the objective function is estimated using a finite difference scheme with a step size of 10^{-4}. In order to seed the search, the needle origin is arbitrarily placed inside the ROI so long as the entire needle lies inside the ROI. The search terminates if the relative change in $|\boldsymbol{\theta}|$ or $\mathcal{J}(\boldsymbol{\theta})$ between iterations were less than 10^{-3} or 10^{-4}, respectively.

Sensitivity analysis

In order to study the sensitivity of the optimized needle placements, the x and y coordinates of $\boldsymbol{\theta}$ are perturbed according to a Gaussian distribution,

$prb[\boldsymbol{\theta}] = G\left(x, y; x_{opt}, y_{opt}, s_x, s_y\right)$. The following two distributions are then computed. One is the expected Arrhenius survival distribution in the region of interest at the end of ablation:

$$\varpi(\mathbf{x}) = \int \omega(\mathbf{x};\boldsymbol{\theta})\, prb[\boldsymbol{\theta}]\, d\boldsymbol{\theta}\,. \tag{4.9}$$

The second is the frequency of obtaining an Arrhenius survival fraction below a threshold, ω_0:

$$\overline{S}(\mathbf{x}) = \int S(\mathbf{x};\boldsymbol{\theta})\, prb[\boldsymbol{\theta}]\, d\boldsymbol{\theta}\,, \tag{4.10}$$

where $S(\mathbf{x})$ is defined to 1 wherever $\omega(\mathbf{x}) \le \omega_0$, and 0 otherwise. In this study, the tissue is considered successfully ablated at below $\omega_0 = 0.01$. Level sets of $\overline{S}$ thus represent regions in space for which ablations can be achieved at those confidence levels over all trial implementations of the plan. For instance, if placement is perfectly accurate, then the 100% level set would coincide with the predicted ablation. Integration for both distributions is performed using a Monte Carlo scheme, in which perturbations are drawn from a Gaussian random number generator.

Simulation Experiments

BEM-FEM validation

In order to test the validity of the BEM-FEM approach described above, a model geometry with an analytic solution to the electrostatic equation was used. The embedded needle was given a 1.0 V Dirichlet boundary condition, whereas the entire boundary of the exterior domain was grounded. The power distribution calculated by solving the electrostatic FEM using the BEM computed current distribution was compared with analytic solutions.

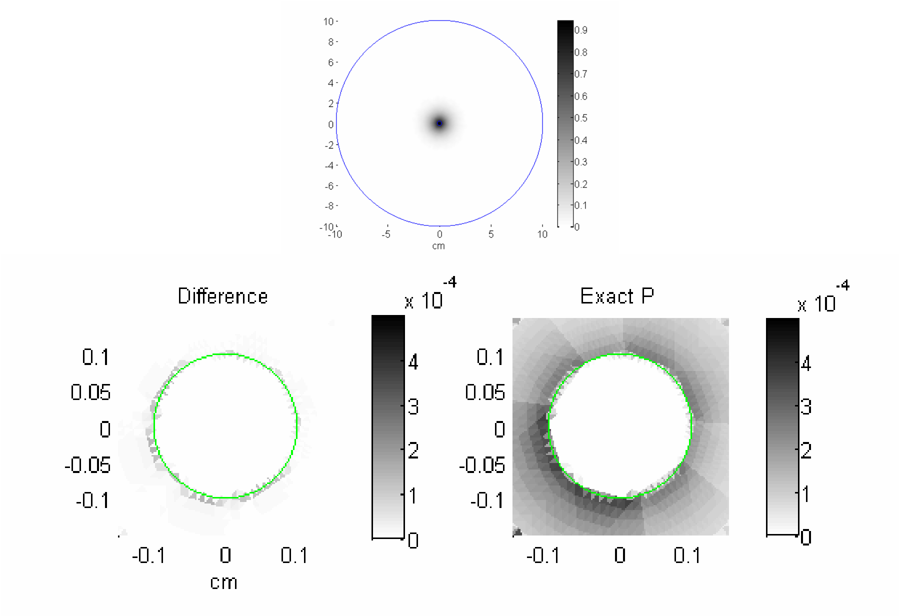

Figure IV-3: BEM-FEM model validation using a geometry with two concentric circles. (*top*) Temperature difference from modeling with BEM-FEM computed power distribution versus analytic power distribution (°C), shown for the entire domain. (*bottom left*) The difference in BEM-FEM computed power distribution and analytic power distribution. (*bottom right*) Analytic power distribution, shown around the circular needle.

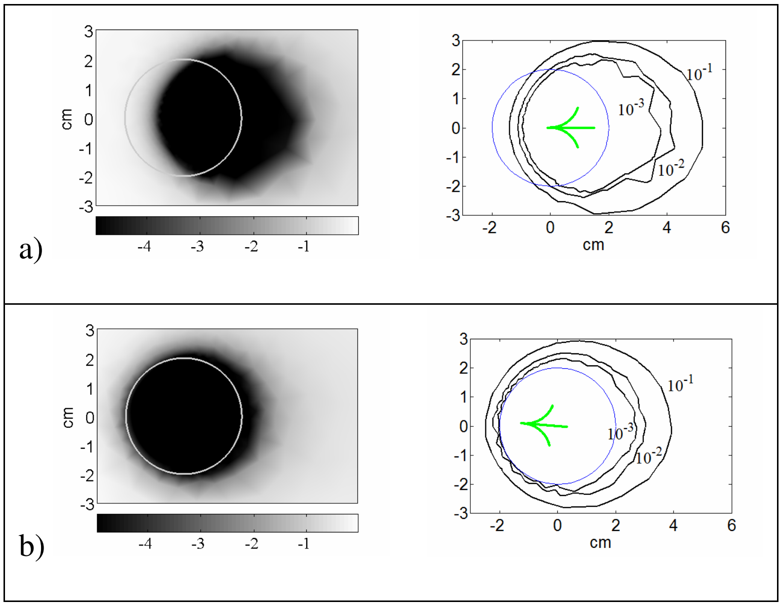

Case 1: a) A plot of $\log_{10} \omega(\mathbf{x})$ for the initial placement and a contour plot of $\log_{10} \omega(\mathbf{x})$; b) similar plots for the optimized needle placement.

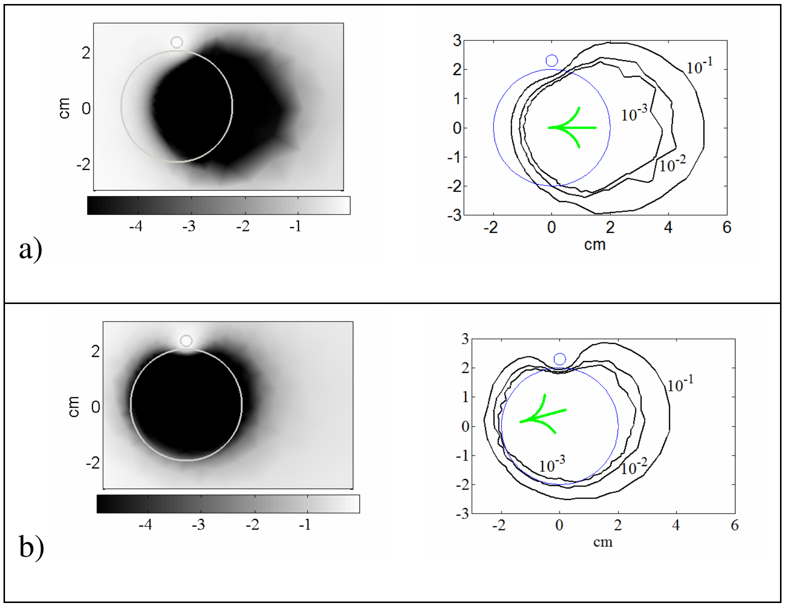

Case 2: a) A plot of $\log_{10} \omega(\mathbf{x})$ for the initial placement and a contour plot of $\log_{10} \omega(\mathbf{x})$; b) similar plots for the optimized needle placement.

Figure IV-4: Simulation results comparing initial and optimized needle placements for two domains.

The results are shown in Figure IV-3. As seen in the figure, the error distribution of the BEM-FEM solution is dependent on the level of mesh discretization. In particular, elements that contain the BEM current sources have higher errors. This error likely reflects the use of a linear basis function in the finite element solution. In order to compare the effects of this error on temperature distribution, an ablation simulation was performed. As described above, a constant power ablation was performed for 10 minutes, and a temperature distribution was obtained at 10 minutes both for the power computed with BEM-FEM and with the analytic solution. The difference in temperature distribution is shown in Figure IV-3. The maximum reported temperature rise at the center of the domain was 32 °C.

Optimization results

Values for the constitutive properties used in our model are listed in [53], with the exception that perfusion is not modeled (*i.e.* $h_b = 0$). For the BEM problem, the boundary and current source were discretized into $N_b = 200$ and $N_s = 360$ segments, respectively. For the FEM problem, the ROI contained 1504 triangles out of 2623 used in the entire domain. At each step of the optimization, the total power deposited in the domain was fixed at 15 W/cm for 10 minutes. The Arrhenius survival fraction was then evaluated 6 minutes (*i.e.* $t_f = 16$ min.) after the power is shut off. All algorithms were implemented using Matlab (MathWorks, Inc.) on a 3.4 GHz Pentium 4 platform with 2 GB RAM. Optimization was attempted for two cases using the prototype model, one modeling the effects of a nearby vessel and one without. Computation times for all cases ranged between 10-15 minutes.

Table IV-1: Changes in needle positions and objective function between initial and optimized results.

Case	Δx (cm)	Δy (cm)	$\Delta\theta$ (deg)	$\mathcal{J}_0$	$\mathcal{J}_{opt}$	Ablation Area (cm^2)
`−vessel`	-1.16	0.08	-4.6	4.2e-2	6.2e-6	20.98
`+vessel`	-1.24	0.16	15.3	5.1e-2	5.6e-4	18.88

The Arrhenius survival distributions for the no-vessel and vessel cases (Case 1 and 2, respectively) are shown in Figure IV-4. Changes in the optimization parameters and objective functions are tabulated in Table IV-1. A comparison of the two cases shows that optimal placements depend on the presence of nearby thermal sinks. In particular, with a nearby vessel, the optimal needle placement is deflected towards the vessel so that the tips of the tines, where the most amount of power is deposited, come closer to the vessel. Despite this adjustment, however, some parts of the ROI around the vessel remain relatively undertreated (i.e. $\omega > 0.01$). Indeed, the value of $\mathcal{J}_{opt}$ is higher than in the no-vessel case. Such a result could be potentially informative in an actual clinical scenario by prompting the need for a change in treatment strategy or additional monitoring of this region after ablation.

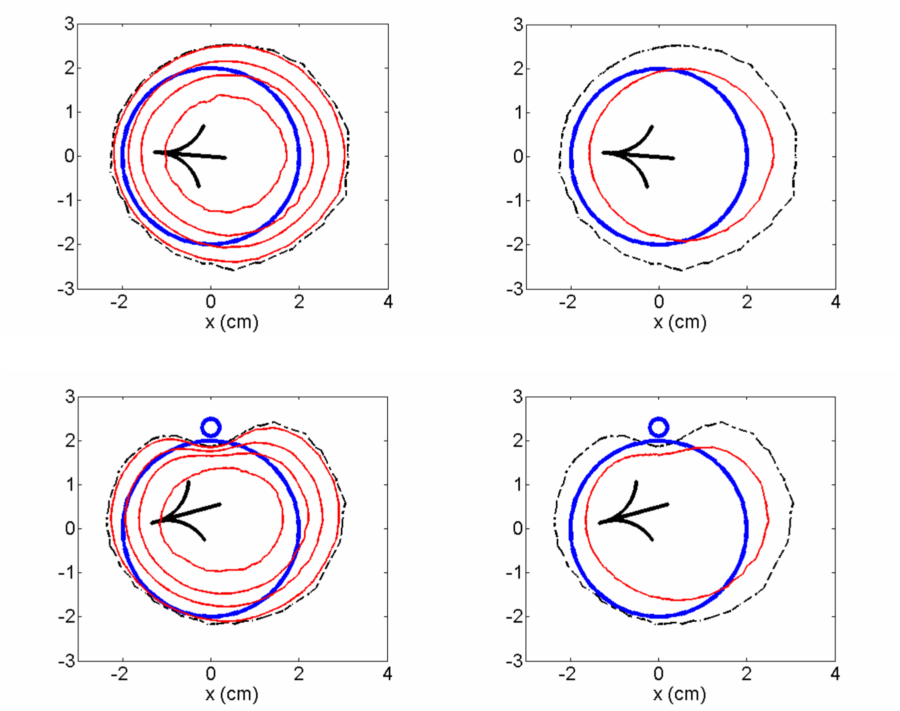

Figure IV-5: Results of Monte Carlo simulation in studying sensitivity of previously optimized needle placements to 5 mm Gaussian error in needle position. (*left column*) Thin solid lines represent level sets of $\overline{S}$ depicted, from outer to inner contour, at 50%, 75%, 90%, and 99% confidence in achieving successful ablation. (*right column*) Thin solid line represents the mean ablation $\overline{\omega}$ at the threshold level ω_0. Results are shown for cases with no vessel (*top row*), and a vessel (*bottom row*). In all diagrams, the dashed line represents the original predicted ablation given by the threshold level ω_0. The thick circular geometries represent the tumor boundary and the vessel, and the optimized needle placement is depicted.

Finally, an observation of the four simulations reveals that the ablation zone is typically not centered about the centroid of the needle. Indeed, the needle is typically placed to the left of the vertical midline of the ROI, and the ablation zone extends preferentially towards ground, located on the right-hand side of the domain. These results suggest the potential importance of the placement of the grounding pad in addition to the placement of the needle in optimizing therapy.

Sensitivity Analysis

In a series of Monte Carlo simulations for each of the vessel and no-vessel cases, the Gaussian localization model was set with standard deviation parameters $s_x = s_y = s$, in which s was varied from 1.0mm to 5.0mm in increments of 1.0mm. Thus, 5 simulations were performed for each domain, and each simulation took approximately 1-2 hours to perform on the platform described above. Figure IV-5 shows the distributions of $\bar{\omega}$ and $\bar{S}$ for the case of $\sigma = 5.0$ mm. As shown in both domains, the mean ablation extents are smaller than that of the initial predicted ablation, and the level sets of $\bar{S}$ at the highest confidence levels fail to overlap the tumor significantly. An interesting observation in the case of the domain with a vessel is that the closest distance from the level sets of $\bar{S}$ to the initial predicted ablation zone is smaller near the vessel than elsewhere. This result indicates that although the vessel deforms the ablation zone, its effect is spatially limited. Indeed, if the vessel were not there, it is likely that sufficient power is still being deposited near the vessel location to generate an ablation that would overlap that region. A possible explanation is that in all perturbations to the position, the needle tips, where most power is deposited, are oriented close to the vessels. If perturbations to orientation are included, the efficiency of ablating near the vessel may decrease. In Figure IV-6, the trends over all error levels are plotted. A notable pattern in the trends is that the rate of decrease in expected ablation areas and tumor coverage is largely the same in both domains, despite the different geometries of the final ablation zone. This pattern may be coincidental with only perturbing the position of the needle, but not its orientation. As a result, the net effect is approximately the same as convolving the initial predicted survival

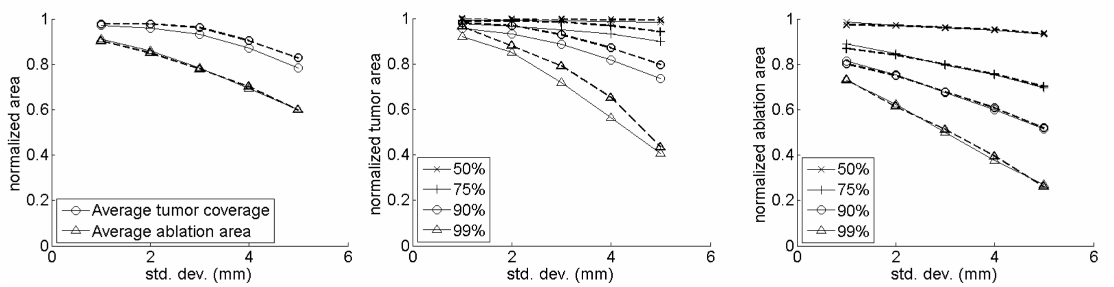

Figure IV-6: (*left*) Areas of expected ablation outcome $\overline{\omega}$ and its overlap with the tumor, normalized by the initial predicted ablation area and the tumor area, respectively. (*middle*) Areas of overlap between level sets of $\overline{S}$ and the tumor, normalized by the tumor area. (*right*) Areas of level sets of $\overline{S}$, normalized by the initial predicted ablation area. In all plots, the solid line refers to the case with a vessel, and the dashed line to the case without.

distribution with the Gaussian kernel used in the Monte Carlo simulation, which would smear the distribution out symmetrically in a manner that reduces the ablation margin.

In general the results show that as the perturbations increase in magnitude, less of the tumor can be expected to be ablated with high confidence. These results thus provide motivation for improving surgical navigation as an indirect means of achieving effectively greater ablation sizes by making a higher percentage of the predicted ablation zone more likely to be achieved per needle placement. These results also indicate that the planning process may benefit from incorporating measures of placement sensitivity into the objective function (*e.g.* local gradient information). Currently, the objective function decreases in value dramatically as soon as the entire region of interest is within the ω_0 level set. Thus, the optimization routine terminates even if the margins of the tumor are close to the ω_0 level set. In a sense, the termination is premature because even though the local gradient magnitude has decreased below tolerance, further optimization is still possible. For instance, in the case of the domain with no vessel, the roughly circular contours shown in Figure IV-5 are not concentric with the tumor. An optimization method informed by sensitivity analysis may further reposition the needle, or may indicate additional ablations to be performed.

Conclusions

We have described a computational framework to optimize needle placement and demonstrated its feasibility in simulations. The method aims to minimize remeshing as a means to reducing computational burden in order to evaluate model simulations for multiple needle placements. This efficiency is achieved by incorporating a current source representation of the RFA needle, the distribution of which is solved by BEM. This current source representation can be integrated into FEMs in a mesh-independent manner. In addition, we have adopted the framework to study the sensitivity of planning to localization errors. The results show that uncertainties in needle placement effectively reduce the expected ablation extents.

CHAPTER V

CONCLUDING REMARKS

Summary of Research

The goal of this research was to develop and evaluate a framework to plan the placement of radiofrequency ablation device. In Chapter II, a method was created to search for the device placement that would maximize the therapeutic goal according to an Arrhenius survival distribution. This work improved on conventional planning techniques, which rely on geometric assumption about the final ablation outcome, by coupling the search with finite element models of ablations. Because the finite element models were based on constitutive equations describing the physical processes governing RFA, this approach had the potential advantage of using physically meaningful and relevant parameters to predict ablation outcomes. Nevertheless, compared to using geometries such as spheres or ellipsoids, models based on FEM solutions were more computationally intensive. Thus, a novel scheme was developed based on the assumption that over small perturbations to the device orientation and position, the overall shape of the ablation would transform rigidly with respect to the device. Reducing the problem in this manner allowed the use of image processing techniques to maximize the overlap of the ablation extents with the designated treatment region. Then, to relax the artificial constraint that the ablation shape is invariant with respect to position in order to account for actual changes in ablation shape that occur because of thermal and electrical boundary conditions, the ablation was periodically updated by resolving the entire system at the last searched device position and orientation. This method was evaluated both for single ablations and multiple ablations. In single ablation scenarios, the method was tested using perturbation analysis that were intended to represent worst scenarios in which the treatment region was as large as the ablation itself. Results suggested that the search was insensitive to roll about the axis of the needle, but was otherwise capable of determining a needle placement that covered the treatment region. In the multiple ablation scenario, a strategy was developed to reduce the complexity of the problem by decomposing the region into separate regions, and planning for each subdomain individually. The combined ablation was capable of ablating more completely than the single ablation. In addition, this result was achieved with fewer ablations than theoretically possible in geometric planning approaches.

Chapter III described the development of a phantom system used to test the accuracy of the model presented in Chapter II, as well as to evaluate the ability of an optically tracked radiofrequency ablation device to predict the extents of the ablation spatially. An agarose-albumin gel phantom was constructed which provided a rigid setting for ablation experiments to be conducted. In order to track the ablation device, a needle holder was built around the shaft of the needle in a manner that would not interfere with the deployed electrodes. Then, a series of calibration steps were described that mapped the location of these electrodes into the coordinate system of the phantom. Comparison between the modeled ablation and the imaged ablation showed that the model correctly predicted at least 90% of the pixels corresponding to coagulated albumin. This accuracy was achieved with the model labeling 20% more pixels ablated than were actually ablated. To determine if these pixel misclassifications could be explained by positional inaccuracy of the needle alone, methods from Chapter II were employed to reposition the needle to maximize the overlap between needle and ablation. The resulting prediction accuracy improved to cover at least 99% of the imaged ablation, and the result was achieved with only a nominal increase in the ablation size. This outcome hinted that the model was itself accurate, and that the model discrepancies were a result of device tracking errors. Analysis of the contours of the Arrhenius distribution showed that the contours tended to agree well with the morphology of the imaged ablation. Further it suggested that the model overprediction may be a result of incorrect threshold choice. Comparison of the FEM model with spherical models also suggested that the FEM models tended to account for a higher percentage of the imaged ablation pixels than spheres over a range of threshold choices and sphere sizes.

Inaccurate placement of the needle, like those observed in Chapter III, motivated the development of the techniques in Chapter IV. In this work, the goal was to study how uncertainties in needle placement affect the reliability of an ablation produced from a treatment plan produced in Chapter II. In particular, the aim was to determine the subset of the predicted ablation region that would be expected at a prescribed confidence level. To achieve this goal, a Monte Carlo scheme was used to evaluate the models for multiple perturbations to an optimal needle placement. As noted in Chapter II, however, the complexity of FEM models precluded the possibility of using this approach. Thus, a reduced model based on FEM-BEM approach was implemented. This method allowed the needle to be represented as a current source which could be directly integrated into a static FEM mesh. Consequently, the preprocessing steps such as mesh generation and matrix assembly involved in FEM methods need only be done once. The result from coupling the FEM-BEM model to a Monte Carlo integration scheme was a probability distribution in space representing the percentage of Monte Carlo trials that achieved successful ablation at any given point in the treatment area. As uncertainty increased, the region of the originally predicted ablation area that could be confidently ablated 90% of the time (*i.e.* over all trials) decreased by as much as 40%. In comparing these probability maps from domains with and without a nearby vessel it was shown that regions near the vessel were potentially less sensitive to positional uncertainties than other regions of the treatment volume. This result suggested that depositing enough electrical power near the vessel was potentially a means of producing ablations that were robust to uncertainties in placement. In general, the sensitivity analysis also indicated that multiple ablation approaches may be required even when a single planned ablation is predicted to overlap the treatment completely.

Future work

Model improvements

Models can be improved to handle more physical phenomena. Of particular interest is further research into modeling the effects of vessels over the relevant clinical ranges, namely those that are greater than 3 mm in diameter. Because the tissue near the vessels is mostly likely to be ablated marginally, a more accurate analysis of the heat transfer in that region could generate a better understanding of the ablation efficacy. Additional high-temperature dynamics, such as water boiling and tissue desiccation may also need to be incorporated. Model improvements may also be achieved by enhancing the performance of any individual computational component of the framework. In particular, the most computationally intensive step in FEM analysis remains the time-stepping scheme used in producing the transient temperature distribution. Methods to solve the nonlinear time-dependent differential equation more efficiently may make tractable the coupling FEM of analysis to Monte Carlo analysis.

Multiple ablations

As indicated in this dissertation, planning multiple ablations is a complex problem and merits further study. The proposed strategy of decomposing the region of interest into subdomains reduces the problem complexity to planning for single ablations. In doing so, however, it is assumed that past ablations have no effect on subsequent ablations. There are potential problems with this approach. First, irreversible changes occur during the course of an ablation. Notably, perfusion in the ablated region remains suppressed because local microvasculature is destroyed. Other permanent changes have been observed in the literature include an altered baseline thermal and electrical conductivity. Furthermore, in clinical applications, it is unlikely that the surgeon waits long enough for the local temperatures to return to body temperature, as is currently assumed in the proposed methods. Having a higher initial temperature distribution means that subsequent ablations are likely to reach boiling temperatures more readily, a scenario in which the presented models become less predictive as additional dynamics come into play. It may be important to incorporate these phenomena into the model in order to quantify the potential synergistic (or detrimental) effects of cumulative ablations.

In vivo validation

Ultimately, this research should proceed into the operating room. Before then, however, a number of studies may be required to evaluate the effects of perfusion on planning. Although a phantom system such as the one described in this research is desirable, little is presently known on how to construct a perfused phantom mimicking organic models. Consequently, *in vivo* animal studies are likely to be the best model system. In these models, however, device placement becomes less well controlled, particularly because of difficulties in coregistering the target organ with the space of the tracking system. Research into navigation in soft-tissue organs such as the liver may help further inform the planning process. In particular, sensitivity analysis to placement error may be better constrained to model the mechanics involved in targeting a deformable organ with poor anatomical landmarks to be used for coregistration. Retrospective analysis may be a first step towards *in vivo* validation, where the needle is tracked during use, and then a model is executed based on the positional data to compare with post-ablation imaging analysis.

BIBLIOGRAPHY

1. Ferlay, J., et al., *GLOBOCAN 2002: Cancer Incidence, Mortality and Prevalence Worldwide*. 2004, International Agency for Research on Cancer (http://www-dep.iarc.fr/): Lyon, France.

2. Bosch, F.X., J. Ribes, and J. Borras, *Epidemiology of primary liver cancer.* Seminars in Liver Disease, 1999. **19**(3): p. 271-285.

3. Kew, M.C., *Epidemiology of hepatocellular carcinoma.* Toxicology, 2002. **181**: p. 35-38.

4. McGahan, J.P. and G.D. Dodd, *Radiofrequency ablation of the liver: Current status.* American Journal of Roentgenology, 2001. **176**(1): p. 3-16.

5. El-Serag, H.B. and A.C. Mason, *Rising incidence of hepatocellular carcinoma in the United States.* N Engl J Med, 1999. **340**(10): p. 745-50.

6. Kew, M.C., *Hepatic Tumors and Cysts*, in *Sleisenger & Fordtran's gastrointestinal and liver disease pathophysiology, diagnosis, management*, MD Consult LLC., Editor. 2002, MD Consult LLC: St. Louis, MO. p. 1577-1593.

7. Jemal, A., et al., *Cancer statistics, 2004.* CA Cancer J Clin, 2004. **54**(1): p. 8-29.

8. Bentrem, D.J., R.P. DeMatteo, and L.H. Blumgart, *Surgical Therapy for Metastatic Disease to the Liver.* Annu Rev Med, 2004.

9. Ng, K.K.C., et al., *Thermal ablative therapy for malignant liver tumors: A critical appraisal.* Journal of Gastroenterology and Hepatology, 2003. **18**(6): p. 616-629.

10. Curley, S.A., et al., *Surgical treatment of colorectal cancer metastasis.* Cancer Metastasis Rev, 2004. **23**(1-2): p. 165-82.

11. Cady, B., et al., *Surgical margin in hepatic resection for colorectal metastasis: a critical and improvable determinant of outcome.* Ann Surg, 1998. **227**(4): p. 566-71.

12. Elias, D., et al., *Results of 136 curative hepatectomies with a safety margin of less than 10 mm for colorectal metastases.* J Surg Oncol, 1998. **69**(2): p. 88-93.

13. Choti, M.A., *Surgical management of hepatocellular carcinoma: resection and ablation.* J Vasc Interv Radiol, 2002. **13**(9 Pt 2): p. S197-203.

14. Curley, S.A., *Radiofrequency ablation of malignant liver tumors.* Oncologist, 2001. **6**(1): p. 14-23.

15. Ng, K.K. and R.T. Poon, *Radiofrequency ablation for malignant liver tumor.* Surg Oncol, 2005. **14**(1): p. 41-52.

16. Shetty, S.K., et al., *Cost-effectiveness of percutaneous radiofrequency ablation for malignant hepatic neoplasms.* J Vasc Interv Radiol, 2001. **12**(7): p. 823-33.

17. Mulier, S., et al., *Complications of radiofrequency coagulation of liver tumours.* British Journal of Surgery, 2002. **89**(10): p. 1206-1222.

18. Curley, S.A., et al., *Early and late complications after radiofrequency ablation of malignant liver tumors in 608 patients.* Ann Surg, 2004. **239**(4): p. 450-8.

19. Hong, S.N., et al., *Comparing the outcomes of radiofrequency ablation and surgery in patients with a single small hepatocellular carcinoma and well-preserved hepatic function.* J Clin Gastroenterol, 2005. **39**(3): p. 247-52.

20. Haemmerich, D. and F.T. Lee, Jr., *Multiple applicator approaches for radiofrequency and microwave ablation.* Int J Hyperthermia, 2005. **21**(2): p. 93-106.

21. Goldberg, S.N., *Radiofrequency tumor ablation: principles and techniques.* Eur J Ultrasound, 2001. **13**(2): p. 129-47.

22. Goldberg, S.N., G.S. Gazelle, and P.R. Mueller, *Thermal ablation therapy for focal malignancy: a unified approach to underlying principles, techniques, and diagnostic imaging guidance.* AJR Am J Roentgenol, 2000. **174**(2): p. 323-31.

23. Rhim, H., et al., *Essential techniques for successful radio-frequency thermal ablation of malignant hepatic tumors.* Radiographics, 2001. **21 Spec No**: p. S17-35; discussion S36-9.

24. Tanabe, K.K., et al., *Radiofrequency ablation: the experts weigh in.* Cancer, 2004. **100**(3): p. 641-50.

25. Pereira, P.L., et al., *Radiofrequency ablation: in vivo comparison of four commercially available devices in pig livers.* Radiology, 2004. **232**(2): p. 482-90.

26. Lobo, S.M., et al., *Radiofrequency ablation: modeling the enhanced temperature response to adjuvant NaCl pretreatment.* Radiology, 2004. **230**(1): p. 175-82.

27. Haemmerich, D., et al., *Large-volume radiofrequency ablation of ex vivo bovine liver with multiple cooled cluster electrodes.* Radiology, 2005. **234**(2): p. 563-568.

28. Poon, R.T., et al., *Effectiveness of radiofrequency ablation for hepatocellular carcinomas larger than 3 cm in diameter.* Arch Surg, 2004. **139**(3): p. 281-7.

29. Livraghi, T., et al., *Hepatocellular carcinoma: Radio-frequency ablation of medium and large lesions.* Radiology, 2000. **214**(3): p. 761-768.

30. Kuvshinoff, B.W. and D.M. Ota, *Radiofrequency ablation of liver tumors: influence of technique and tumor size.* Surgery, 2002. **132**(4): p. 605-11; discussion 611-2.

31. Lu, D.S., et al., *Effect of vessel size on creation of hepatic radiofrequency lesions in pigs: assessment of the "heat sink" effect.* AJR Am J Roentgenol, 2002. **178**(1): p. 47-51.

32. Lu, D.S., et al., *Influence of large peritumoral vessels on outcome of radiofrequency ablation of liver tumors.* J Vasc Interv Radiol, 2003. **14**(10): p. 1267-74.

33. Komorizono, Y., et al., *Risk factors for local recurrence of small hepatocellular carcinoma tumors after a single session, single application of percutaneous radiofrequency ablation.* Cancer, 2003. **97**(5): p. 1253-1262.

34. Dodd, G.D., 3rd, et al., *Radiofrequency thermal ablation: computer analysis of the size of the thermal injury created by overlapping ablations.* AJR Am J Roentgenol, 2001. **177**(4): p. 777-82.

35. Khajanchee, Y.S., et al., *A mathematical model for preoperative planning of radiofrequency ablation of hepatic tumors.* Surg Endosc, 2004. **18**(4): p. 696-701.

36. Scott, D.J., et al., *Accuracy and effectiveness of laparoscopic vs open hepatic radiofrequency ablation.* Surgical Endoscopy-Ultrasound and Interventional Techniques, 2001. **15**(2): p. 135-140.

37. Antoch, G., et al., *Value of CT volume imaging for optimal placement of radiofrequency ablation probes in liver lesions.* Journal of Vascular and Interventional Radiology, 2002. **13**(11): p. 1155-1161.

38. Rose, S.C., et al., *Value of three-dimensional US for optimizing guidance for ablating focal liver tumors.* Journal of Vascular and Interventional Radiology, 2001. **12**(4): p. 507-515.

39. Sjolie, E., et al., *3D ultrasound-based navigation for radiofrequency thermal ablation in the treatment of liver malignancies.* Surgical Endoscopy and Other Interventional Techniques, 2003. **17**(6): p. 933-938.

40. Boctor, E.M., et al. *Tracked 3D ultrasound in radio-frequency liver ablation*. in *Medical Imaging 2003: Ultrasonic Imaging and Signal Processing*. 2003. San Jose, CA: Proc. SPIE.

41. Penney, G., et al. *An Overview of an Ultrasound to CT or MR Registration Algorithm for use in Thermal Ablation of Liver Metastases*. in *Medical Image Understanding and Analysis 2001*. 2001. University of Birmingham, UK.

42. Cash, D.M., et al., *Incorporation of a laser range scanner into image-guided liver surgery: surface acquisition, registration, and tracking.* Med Phys, 2003. **30**(7): p. 1671-82.

43. Herline, A.J., et al., *Image-guided surgery: preliminary feasibility studies of frameless stereotactic liver surgery.* Arch Surg, 1999. **134**(6): p. 644-9; discussion 649-50.

44. Butz, T., et al., *Pre- and intra-operative planning and simulation of percutaneous tumor ablation*, in *Medical Image Computing and Computer-Assisted Intervention - Miccai 2000*. 2000. p. 317-326.

45. Villard, C., et al. *RF-Sim: a Treatment Planning Tool for Radiofrequency Ablation of Hepatic Tumors*. in *Seventh International Conference on Information Visualization*. 2003. London, England: IEEE.

46. Villard, C., et al., *Virtual radiofrequency ablation of liver tumors*, in *Surgery Simulation and Soft Tissue Modeling, Proceedings*. 2003. p. 366-374.

47. Groemer, H., *Coverings and packings by sequences of convex sets*, in *Annals of the New York Academy of Sciences, v. 440*, R. Pollack, Editor. 1985, New York Academy of Sciences: New York, N.Y. p. 262-278.

48. Toth, F., *Packing and covering*, in *Handbook of discrete and computational geometry*, J. O'Rourke, Editor. 1997, CRC Press: Boca Raton. p. 19-41.

49. Okabe, A., *Spatial tessellations : concepts and applications of Voronoi diagrams*. 2nd ed. Wiley series in probability and statistics. 2000, Chichester ; New York: Wiley. xii, 671 p.

50. Rogers, C.A., *Packing and covering*. 1964, New York: Cambridge University Press. viii, 111 p.

51. Fowler, R.J., M.S. Paterson, and S.L. Tanimoto, *Optimal Packing and Covering in the Plane Are Np-Complete.* Information Processing Letters, 1981. **12**(3): p. 133-137.

52. Breen, M.S., et al., *Radiofrequency thermal ablation: correlation of hyperacute MR lesion images with tissue response.* J Magn Reson Imaging, 2004. **20**(3): p. 475-86.

53. Chang, I.A. and U.D. Nguyen, *Thermal modeling of lesion growth with radiofrequency ablation devices.* Biomed Eng Online, 2004. **3**(1): p. 27.

54. Arkin, H., L.X. Xu, and K.R. Holmes, *Recent Developments in Modeling Heat-Transfer in Blood-Perfused Tissues.* Ieee Transactions on Biomedical Engineering, 1994. **41**(2): p. 97-107.

55. Hayes, L.J., et al., *Prediction of transient temperature fields and cumulative tissue destruction for radio frequency heating of a tumor.* Med Phys, 1985. **12**(6): p. 684-92.

56. Haemmerich, D., et al., *Finite-element analysis of hepatic multiple probe radio-frequency ablation.* IEEE Transactions on Biomedical Engineering, 2002. **49**(8): p. 836-842.

57. Ryan, T.P., et al. *Tissue Electrical Properties as a function of thermal dose for use in a finite element model.* in *1997 International Mechanical Engineering Congress and Exposition*. 1997. Dallas, Texas: American Society of Mechanical Engineers.

58. Chang, I., *Finite element analysis of hepatic radiofrequency ablation probes using temperature-dependent electrical conductivity.* Biomed Eng Online, 2003. **2**(1): p. 12.

59. Pop, M., et al., *Changes in dielectric properties at 460 kHz of kidney and fat during heating: importance for radio-frequency thermal therapy.* Phys Med Biol, 2003. **48**(15): p. 2509-25.

60. Consiglieri, L., I. dos Santos, and D. Haemmerich, *Theoretical analysis of the heat convection coefficient in large vessels and the significance for thermal ablative therapies.* Physics in Medicine and Biology, 2003. **48**(24): p. 4125-4134.

61. Whelan, W.M. and D.R. Wyman, *Dynamic modeling of interstitial laser photocoagulation: Implications for lesion formation in liver in vivo.* Lasers in Surgery and Medicine, 1999. **24**(3): p. 202-208.

62. Baissalov, R., et al., *Simultaneous optimization of cryoprobe placement and thermal protocol for cryosurgery.* Phys Med Biol, 2001. **46**(7): p. 1799-814.

63. Baissalov, R., et al., *A semi-empirical treatment planning model for optimization of multiprobe cryosurgery.* Phys Med Biol, 2000. **45**(5): p. 1085-98.

64. Lung, D.C., T.F. Stahovich, and Y. Rabin, *Computerized planning for multiprobe cryosurgery using a force-field analogy.* Comput Methods Biomech Biomed Engin, 2004. **7**(2): p. 101-10.

65. Pacella, C.M., et al., *Laser thermal ablation in the treatment of small hepatocellular carcinoma: results in 74 patients.* Radiology, 2001. **221**(3): p. 712-20.

66. Sotsky, T.K. and T.S. Ravikumar, *Cryotherapy in the treatment of liver metastases from colorectal cancer.* Semin Oncol, 2002. **29**(2): p. 183-91.

67. Kennedy, J.E., G.R. Ter Haar, and D. Cranston, *High intensity focused ultrasound: surgery of the future?* Br J Radiol, 2003. **76**(909): p. 590-9.

68. Wood, T.F., et al., *Radiofrequency ablatian of 231 unresectable hepatic tumors: Indications, limitations, and complications.* Annals of Surgical Oncology, 2000. **7**(8): p. 593-600.

69. Chen, M.H., et al., *Large liver tumors: protocol for radiofrequency ablation and its clinical application in 110 patients--mathematic model, overlapping mode, and electrode placement process.* Radiology, 2004. **232**(1): p. 260-71.

70. Villard, C., L. Soler, and A. Gangi, *Radiofrequency ablation of hepatic tumors: simulation, planning, and contribution of virtual reality and haptics.* Comput Methods Biomech Biomed Engin, 2005. **8**(4): p. 215-27.

71. Mulier, S., et al., *Size and geometry of hepatic radiofrequency lesions.* Eur J Surg Oncol, 2003. **29**(10): p. 867-78.

72. Si, H., *Tetgen*. 2005: Berlin, Germany.

73. Tungjitkusolmun, S., et al., *Three-dimensional finite-element analyses for radio-frequency hepatic tumor ablation.* IEEE Transactions on Biomedical Engineering, 2002. **49**(1): p. 3-9.

74. Ryan, T.P. and S.H. Goldberg. *Comparison of Simulation and Experimental Results for RF Thermal Treatment Devices with or without Cooling*. in *Proceedings of thermal treatment of tissue with image guidance*. 1999. San Jose, CA: SPIE.

75. Schwarzmaier, H.J., et al., *Treatment planning for MRI-guided laser-induced interstitial thermotherapy of brain tumors--the role of blood perfusion.* J Magn Reson Imaging, 1998. **8**(1): p. 121-7.

76. Lin, W.C., C. Buttemere, and A. Mahadevan-Jansen, *Effect of thermal damage on the in vitro optical and fluorescence characteristics of liver tissue's.* Ieee Journal of Selected Topics in Quantum Electronics, 2003. **9**(2): p. 162-170.

77. Pethig, R. and D.B. Kell, *The passive electrical properties of biological systems: their significance in physiology, biophysics and biotechnology.* Phys Med Biol, 1987. **32**(8): p. 933-70.

78. Kim, B.M., et al., *Nonlinear finite-element analysis of the role of dynamic changes in blood perfusion and optical properties in laser coagulation of tissue.* IEEE Journal of Selected Topics in Quantum Electronics, 1996. **2**(4): p. 922-933.

79. Shahidi, A.V. and P. Savard, *A finite element model for radiofrequency ablation of the myocardium.* IEEE Trans Biomed Eng, 1994. **41**(10): p. 963-8.

80. Balay, S., et al., *PETSc*. 2005.

81. Haemmerich, D., et al., *Hepatic bipolar radio-frequency ablation between separated multiprong electrodes.* Biomedical Engineering, IEEE Transactions on, 2001. **48**(10): p. 1145-1152.

82. Fletcher, R., *Practical methods of optimization*. 2nd ed. 1987, Chichester ; New York: Wiley. xiv, 436 p.

83. Sheu, T.W., et al., *Three-dimensional analysis for radio-frequency ablation of liver tumor with blood perfusion effect.* Comput Methods Biomech Biomed Engin, 2005. **8**(4): p. 229-40.

84. Banovac, F., et al., *Precision targeting of liver lesions using a novel electromagnetic navigation device in physiologic phantom and swine.* Med Phys, 2005. **32**(8): p. 2698-705.

85. Maurer, C.R., Jr., et al., *Registration of head volume images using implantable fiducial markers.* IEEE Trans Med Imaging, 1997. **16**(4): p. 447-62.

86. Iizuka, M.N., M.D. Sherar, and I.A. Vitkin, *Optical phantom materials for near infrared laser photocoagulation studies.* Lasers Surg Med, 1999. **25**(2): p. 159-69.

87. Harris, S.S., D. Hallahan, and J. Robert L. Galloway. *A technique for validating image-guided gene therapy*. in *Medical Imaging 2003: Visualization, Image-Guided Procedures, and Display*. 2003: SPIE.

88. Cash, D.M., et al., *Compensating for intraoperative soft-tissue deformations using incomplete surface data and finite elements.* IEEE Trans Med Imaging, 2005. **24**(11): p. 1479-91.

89. Brebbia, C.A. and J. Dominquez, *Boundary elements : an introductory course*. 2nd ed. 1992, New York: Computational Mechanics Publications. 313 p.

90. O'Rourke, J., *Computational geometry in C*. 2nd ed. 1998, Cambridge, UK, ; New York, NY, USA: Cambridge University Press. xiii, 376 p.

91. Haemmerich, D. and J.G. Webster, *Automatic control of finite element models for temperature-controlled radiofrequency ablation.* Biomed Eng Online, 2005. **4**(1): p. 42.